Numerical simulations of 2-D steady and unsteady breaking waves

Guido Lupieri[1], Giorgio Contento[2]

Department of Engineering and Architecture, University of Trieste, via Valerio, 10, 34127 Trieste, Italy

Abstract

In this work we analyze by means of numerical simulations the features of breaking of two dimensional free surface waves induced by a body or a sloping bottom. The sample cases selected for the simulations characterize different aspects of wave breaking, thus they are supposed to represent rather widely a problem of large interest for ship hydrodynamics and ocean engineering applications. The simulations considered are: wave breaking induced by a fully submerged hydrofoil towed in calm water at constant speed; shallow water waves breaking on a sloping beach in spilling and plunging mode; regular intermediate depth waves breaking gently over a weakly submerged horizontal circular cylinder at a low Keulegan-Carpenter number. Each simulated case is supported by detailed comparisons with experimental data in time and frequency domain. The results presented have been obtained adopting a standard RANS approach. They show a generally good reproduction of the wave breaking characteristics even though it is rather clear that there is a case dependent potential loss of accuracy in the presence of pronounced foamy flow.

Keywords: breaking waves, steady and unsteady breakers, turbulence models, OpenFOAM.

[1]Corresponding author. Tel.: +39-040-5582955, e-mail address: glupieri@units.it
[2]Second author. Tel.: +39-040-5583424, e-mail address: contento@units.it

1. Introduction

Wave breaking plays an important role in ship/marine hydrodynamics and in offshore/coastal engineering as it relates, among others, to wave loads on floating or fixed bodies, to energy loss of wind waves and to ship resistance in calm water or in a seaway. Wave breaking is also related to the ultimate behavior of steep deep water waves under modulational (Benjamin-Feir) instability. In this respect, the scientific community involved in free surface hydrodynamics has fed both laboratory measurements and numerical studies. RANS models still represent the bulk of the numerical simulations. The understanding of the actual effect of turbulence in the two-phase flow resulting from breaking is still a challenging problem, both in experimental measurements and in numerical simulations. For instance, simplified models have been developed and applied to overcome the difficulties in handling the typical unsteady foamy flow of the breakers. Muscari and Di Mascio (2004) have proposed a wave breaking model parameterization useful to account for average energy loss in the RANS computations of ship resistance in calm water.

The simulation of two-dimensional breaking waves is often considered as a common starting point for understanding, handling or calibrating a new solver for the dynamics of interface problems with breaking. A common technique for modeling 2-D flows in turbulent regime is RANS approach. In this case, there are at least three relevant aspects to take care of: a) the parameterization of the flow with turbulence models acts as an intrinsic cut-off of the high frequency space/time fluctuations and therefore it allows to capture only some characteristics of the flow (Iaccarino et al., 2003); b) turbulence modeling in 2-D is always a thorny charge because of a 3-D intrinsic nature of the phenomenon (Lilly, 1969), and even if the most popular RANS turbulence models, from Spalart-Allmaras to $k-\epsilon$, have been extensively calibrated and adopted also in 2-D flows (Menter, 1994), the whole energy cascade mechanism is not straightly accounted for and this aspect could still reveal further weaknesses in the solution (Zhao et al., 2004), c) since turbulence is a multi-scale phenomenon, a range of lengths (for

instance the sizes of the vortices eventually present in the flow) and frequencies is present but, when designing a RANS simulation, it is request to identify a unique reference value, for instance, for specific dissipation or turbulent kinetic energy (namely the amount of fluctuations in the velocity field) (Zhao and Armfield, 2010). Moreover most of the standard experiments in the marine hydrodynamics field are conducted at relatively low Reynolds numbers, typically of order of $10^5 \div 10^6$. In these cases, the adoption of RANS methods can lead to over-smoothed free surface profiles, moving the position of the crests/hollows, inhibiting the entrapment of air bubbles and removing implicitly high frequency terms in the flow field and in the free surface elevation.

Starting from the considerations above, the goal of this work is to reproduce some of the main characteristics of complex two-phase flows with breaking, namely free surface elevation, its macro-time scales and pressure field, adopting a standard RANS approach. Solid experimental data are used as reference. The numerical experiments are executed with and without modeling of turbulence, in order to evince, when time and space resolutions are adequate, useful indications on the same targets.

Consistently with the RANS approach, the main instruments for the analysis are averages (over a number of periods and in phase), reproducing here the free surface in statistically meaningful terms. This is done in all cases analyzed. Furthermore, in order to clarify some aspect of the phenomena or to refer to solid experimental and numerical results from other authors, time series at fixed gauges and snapshots will be presented too.

The selected numerical simulations are:

Case I: steady and unsteady breaking induced by a fully submerged hydrofoil at constant speed in calm water;

Case II: ultra shallow water cnoidal waves breaking in spilling and plunging mode on a sloping beach (ramp);

Case III: breaking of intermediate water depth regular waves, induced by a weakly submerged horizontal circular cylinder at a low Keulegan-Carpenter number.

The first two simulations (Case I and Case II) are supported by the results of celebrated experiments, Duncan (1983, 2001, 1981), De Blasi et al. (2000) and Ting and Kirby (1994, 1995, 1996) respectively, whereas Case III has been previously studied in the hydrodynamic laboratory of the University of Trieste by one of the authors (Contento and Codiglia, 2001).

The cases selected characterize different aspects of wave breaking induced by a solid boundary/body, thus they are supposed to represent a rather wide variety on a problem of interest for engineering applications.

In the first case, a submerged 2D hydrofoil travels in steady incident flow, generating a wave train. Depending on the Froude number, on the foil submergence and on the angle of attach, the wave train may ultimately break. The incident flow is originally in a laminar regime but breaking makes it locally turbulent. Furthermore the breaker has been observed to pulsate back-and-forth with a well-defined periodicity that depends on the Froude number (Duncan, 1981, 1983, 2001).

In the second case, there is no body inducing breaking. Cnoidal waves, generated by a wavemaking boundary, travel and break on a sloping ramp. Depending on the characteristics of the incident wave, two different types of breaking events may take place, spilling and plunging breakers (Ting and Kirby, 1994, 1995, 1996).

In the third case, a deep water regular wave train generated by a wavemaking boundary, breaks gently on a weakly submerged circular cylinder. Furthermore, the specific case examined is characterized by a low Keulegan Carpenter number and the wave-body interaction leads to a steady streaming around the cylinder surface that induces a pressure field playing a crucial role in the surface elevation as a suction effect on the wave throats and breaking. This has been observed experimentally by Contento and Codiglia (2001).

The paper is organized as follows:

- in Sec. 2 and 3 the mathematical method and the numerical approach are described briefly;

- in Sec. 4 to 6 each physical problem is initially outlined with references to previous studies, then providing details on the computational set up; finally the specific results of interest are shown with comments.

The tool used for this investigation is the OpenFOAM library (2012). The $k-\omega SST$ of Menter (1994) has been considered for turbulence modeling. In this Finite Volume library, the solver for the problems enounced is **interFoam** that includes, as standard for the treatment of free surface fluxes, the Volume Of Fluid technique of Hirt and Nichols (1981). In this work the library has been enriched by a numerical wave absorber designed according to Clement (1996), Smith (2009), Wang et al. (2007) and added to avoid undesired reflections of waves from the boundaries. A wavemaking boundary has been implemented as well.

2. Mathematical model

The governing equations for incompressible Newtonian fluid are the momentum and the mass conservation equation:

$$\frac{\partial(\rho u_i)}{\partial t} + \frac{\partial(\rho u_j u_i)}{\partial x_j} = -\frac{\partial p}{\partial x_i} + \frac{\partial}{\partial x_j}\left(\mu\left(\frac{\partial u_i}{\partial x_j} + \frac{\partial u_j}{\partial x_i}\right)\right) \tag{1}$$

$$\frac{\partial u_i}{\partial x_i} = 0 \tag{2}$$

where ρ is the fluid density, u_i is the velocity component, p is pressure without hydrostatic term, μ is the dynamic viscosity, t and x_i the time/space independent variables.

Broadly speaking, for large Reynolds numbers the Navier-Stokes equations can be reformulated in terms of Reynolds averages. Then, to achieve the closure of the new set of equations, additional equations are added in order to redefine the eddy viscosity. In this paper, the turbulence model in use is the $k-\omega$ Shear Stress Transport (Menter, 1994) that consists of two extra transport equations, for the turbulent kinetic energy k and for the specific turbulent dissipation ω

respectively. Being interested in two phase flows (a coupled air-water interface system), it is possible to deal with interface capturing methods such as the VOF technique of Hirt and Nichols (1981). The idea is to use a scalar function α to represent the phase of the fluid in each cell, therefore for the viscosity μ and the density ρ in Navier-Stokes equations we have:

$$\begin{cases} \mu = \mu_{water}\alpha + \mu_{air}(1-\alpha) \\ \rho = \rho_{water}\alpha + \rho_{air}(1-\alpha) \end{cases} \tag{3}$$

For the scalar function α the following equation holds:

$$\frac{\partial \alpha}{\partial t} + \frac{\partial (u_i \alpha)}{\partial x_i} = 0 \tag{4}$$

The function α is bounded between 1 (if only water is present in a control volume) and 0 (if only air is present) over an extremely small layer. This can lead to numerical difficulties associated with the discretization of the convection term in Eq.(4). This in turn results in smearing of the interface. Following Rusche (2002) and Maki (2011), we have used a modified transport equation with an additional convective term that serves to keep the interface sharp:

$$\frac{\partial \alpha}{\partial t} + \frac{\partial (u_i \alpha)}{\partial x_i} + \frac{\partial (w_i \alpha)}{\partial x_i} = 0 \tag{5}$$

where w_i is an artificial velocity field that is directed normal to and towards the interface. The relative magnitude of the artificial velocity is determined with the following expression:

$$w_i = K_c n_i^* \max \frac{|n_i^* F_l|}{|S_i|} \tag{6}$$

where K_c is an adjustable coefficient that determines the magnitude of the compression, n_i^* is the interface unit normal vector, F_l is the flux and S_i is the surface area vector.

These equations complete the mathematical formulation of the two phase flow model. In the following, unless differently specified, the nominal free surface elevation (air-water interface) is referred to $\alpha = 0.5$. It has been shown in

the literature (Chen et al. (2014), Maki (2011)) that Eq.(5) allows mass conservation at a very reasonable level. For the Case III presented below (taken as representative), after approximately 20 periods of the incident wave, the relative variation of the mass is of order of 10^{-3}.

3. Numerical method

The numerical tool used for this investigation is the OpenFOAM library (2012). The Navier-Stokes and free surface equations above are solved over a finite volume using the schemes summarized in Table 1, based on a 2^{nd} order Gaussian integration. The pressure-velocity coupling is achieved using a PISO algorithm. Euler explicit scheme is adopted to march forward in time. The free-surface location is computed using the multidimensional universal limited for explicit solution method (MULES).

As far as wave generation and absorption within the OpenFOAM library is concerned, the work of Jacobsen et al. (2012), Higuera et al. (2013a) and Higuera et al. (2013b) is worth mentioning. In the present work we have implemented our own wave generation as follows:

- we have specified the fluid velocity at the wave-making boundary, derived from a suitable wave theory, leaving the wave elevation free at the boundary cells because of the presence of the unavoidable evanescent modes and possible local disturbances; this method does not cause any serious spurious wave and furthermore it allows a detailed wave calibration;

- for Case II, i.e. ultra shallow water waves, we have used the cnoidal wave model (Fenton, 1998), consistently with what had been done in the work of Xie (2013);

- for Case III, i.e. regular waves in intermediate water depth, we have adopted an "Airy model" conveniently extrapolated above the mean free surface level to account for finite amplitude wave elevation and evanescent modes. This method would lead to a mean positive flux across that boundary during a complete wave period. Therefore at each time step the inlet velocity profile has been corrected

over the whole height with a time dependent function (derived analytically) that keeps the net flux over a whole period at an extremely low level. A time domain and frequency domain analysis of the wave elevation conducted at the cylinder axis position without the submerged cylinder (target wave) have been systematically used to control the incident wave characteristics at the target station (namely height and harmonic terms) and compared with those obtained in our physical wave basin. For Case III, the target value (experimental) is H = 0.127 m, attained value H = 0.126 m, error less than 1%.

Due to the intrinsic strong conservative nature of free surface wave energy, the numerical simulation of waves unavoidably leads to tackle the problem of the limited dimensions of the computing domain. Depending on the BC used at the outlet, totally or partially reflected waves can occur, with evident effects on the pollution of the numerical experiment. To prevent this, a variety of numerical dissipation tools have been developed. The method proposed by Higuera et al. (2013a) has been shown to work really fine for shallow water waves whereas the reflection coefficient in intermediate water depth has been shown to be around 10%, at least for the cases presented in that paper. Alternatively, an absorbing layer can be added over a portion of the domain. It reduces reasonably the wave reflection at the boundary, keeps the effect for a wide range of frequencies provided the beach length is set longer than the typical wavelength of the longest target wave in the spectrum (Clement (1996), Smith (2009),Wang et al. (2007)). However this method is slightly less efficient from the computational point of view since it increases the size of the domain. In our simulations, Case I and Case III specifically, data windowing has been also applied to the time series of the simulations, according to the group velocity of the dominant wave. This has guaranteed highly non-polluted wave characteristics.

For viscous flows an artificial viscosity term in the form of $\rho\alpha\nu_d u_i$ is introduced in the momentum equation Eq.(7) (Wang et al., 2007), where the artificial viscosity function ν_d depends on the longitudinal position x. An ideal case is shown in Fig. 1 where a target wave train is damped in the absorbing region (in gray).

$$\frac{\partial(\rho u_i)}{\partial t} + \frac{\partial(\rho u_j u_i)}{\partial x_j} = -\frac{\partial p}{\partial x_i} + \frac{\partial}{\partial x_j}\left(\mu\left(\frac{\partial u_i}{\partial x_j} + \frac{\partial u_j}{\partial x_i}\right)\right) - \rho\alpha\nu_d(x)u_i \qquad (7)$$

The artificial viscosity function starts from zero at a given location x_{start} in the domain and smoothly increases to its final value at the outlet, smoothness at x_{start} being mandatory to prevent reflections at the beginning of the sponge layer. According to Clement (1996) and Smith (2009), a 3^{rd} order polynomial can be used:

$$\nu_d(x) = \begin{cases} 0 & \text{if } x < x_{start} \\ a(x - x_{start})^3 + b(x - x_{start})^2 + c(x - x_{start}) & \text{if } x > x_{start} \end{cases} \qquad (8)$$

and $a = -2(\nu_{d,max} - ML)/(L^3)$, $b = -\frac{3}{2}aL$ and $c = M$.

The starting location x_{start} of the sponge layer, $\nu_{d,MAX}$ the maximum value of the artificial viscosity function, the slope M of the cubic function at x_{start}, the length of the layer L are user specified. The intensity of the artificial viscosity function depends upon the amount of the wave energy to be dissipated and therefore it must be tuned properly. Consistently with the mentioned literature, in this work we have adopted the following setting: $L = 2\lambda$ where λ is the typical wave length, $M = 0.01$ and $\nu_{d,MAX} = 100$.

As far as the numerical uncertainty U_N is concerned, U_N is here evaluated as suggested by Muscari and Di Mascio (2004) and Roache (1997):

$$U_N = \sqrt{U_{N_H}^2 + U_{N_{IT}}^2} \qquad (9)$$

$U_{N_{IT}}$ takes into account an incomplete iterative convergence:

$$U_{N_{IT}} = \frac{\Delta f}{2} \qquad (10)$$

where Δf is the amplitude of the oscillation of the solution.

U_{N_H} takes into account the effect of the grid size on a generic variable f, as obtained at fine and medium grid resolution:

$$U_{N_H} = \frac{|f_{fine} - f_{medium}|}{r^{\sigma_t} - 1} \tag{11}$$

Here r is the grid refinement ratio and σ_t is the theoretical convergence order. The actual convergence order σ is evaluated as:

$$\sigma = \frac{1}{log(r)} log(\frac{f_{medium} - f_{coarse}}{f_{fine} - f_{medium}}) \tag{12}$$

An additional source of uncertainty comes from the quasi-periodicity of variable f. In Case I in Sec. 4, the wave train induced by the foil in steady incident flow exhibits a time-dependence, including a quasi-periodic breaking. If f is the free surface elevation at any longitudinal position, consistently with the available experimental data, f is computed as phase averaged over a time window whose length is an integer number of the characteristic period. The overall variability in time of f at any position is then represented by the phase average value and by the averages of the max and min values.

For Cases II and III of Sec. 4, the time dependence of f is introduced explicitly by the periodicity T of the wave generated at the wave-making boundary. In those cases, f is computed at any time $0 < t_0 < T$ averaging the data taken over a finite number of corresponding time instants evenly spaced in time, $t = t_0 + i \cdot T$ for any i.

As sample case, hereafter we refer to Case I in Sec. 4, specifically to Sec. 4.3.2 and Fig. 7 where the smallest submergence of the foil induces a violent breaking. Three grids have been used and the results have been re-sampled in space/time in order to use them consistently in Eq.(9) to Eq.(12). The numerical uncertainty U_N (computed for the fine grid relatively to the medium grid) of the local mean free surface elevation has led to $U_{N_H} \simeq 2 \div 3\%$ in the breaking zone and within few chords downwind the foil position and to $U_{N_H} \simeq 0.001\%$ in the rest of the domain. These small values of the numerical uncertainty show that the mean free surface profile has almost reached grid-independence on the medium grid ($U_{N_H} \to 0$) and that it has reached convergence ($U_{N_{IT}} \to 0$). On the other hand, the overall uncertainty that includes the quasi-periodicity of the free sur-

face elevation, is rather large. The largest values occur in the foamy part of the breaker. In this zone, the vertical distance between the max and min elevations is at least one order of magnitude greater than the numerical uncertainty of the mean local wave elevation U_N, thus the overall uncertainty is dominated by quasi-periodicity issues.

4. Case I: unsteady wave breaking induced by a submerged hydrofoil at constant speed in calm water

4.1. Problem formulation

Duncan (1983, 2001, 1981) has conducted a set of experimental tests on a weakly submerged NACA 0012 hydrofoil towed in calm water at constant speed with relatively low Reynolds numbers Re, where $Re = \frac{\rho U c}{\mu}$. The Froude number is here defined as $Fr = \frac{U}{\sqrt{gc}}$. Fig. 2 shows a schematic representation of the set-up: c is the chord length, U the foil speed, α the angle of attack and h the distance from the bottom. In the experiments, different depths of submergence d of the foil have been tested, keeping h fixed. The free surface profiles have been derived from video recording and presented unfortunately without experimental uncertainty. The wave profiles given by Duncan (1983) are thus supposed to be time averaged profiles that include the presence of foam and of unsteady breaking. The original plots of the free surface profiles are reported in Fig. 3 to ease the discussion below.

The literature related to the numerical reproduction of the experiments of Duncan is rather wide and the difficulties in the correct simulation of the wave profiles of Duncan have been already evidenced and discussed, among others, by Muscari and Di Mascio (2004), by Rhee and Stern (2002) and by Lupieri et al. (2012).

De Blasi et al. (2000) have repeated some of the experiments of Duncan in a circulating channel, measuring the free surface elevation and the flow field by LDV, at a slightly higher Reynolds number. Even in steady flow and non-breaking conditions with $d/c = 1.034$, they could not reproduce experimentally

the longitudinal position of the wave train as measured by Duncan, with differences in the position of the zero-crossings of order of more than half chord length. The height of the first two waves of the measured train was rather different too. In that paper these differences have been related mainly to the free surface boundary layer induced by the circulating channel at the inlet section, i.e. a non-uniform incident flow. They have shown that the smaller incident speed in the free surface boundary layer acts a trigger for breaking, inducing large differences in the longitudinal position of the wave train and in the wave height. This is consistent with the results of Duncan, indeed he succeeded in making a wave train break (Fig. 3(b)) from a stable non-breaking condition (Fig. 3(a)) by simply dragging a cloth on the free surface in front of the foil, inducing a kind of free surface current that travels at the same speed of the foil. In the Duncan experiments the breaker height (Fig. 3(b)) dropped down to approximately half the value of the stable non-breaking case (Fig. 3(a)). Even in non-breaking conditions, De Blasi et al. (2000) have shown that, compared to the characteristic wave height, the uncertainty level of the local wave elevation is around 20%, 25% in breaking conditions, where most of the uncertainty level is concerned with the quasi-periodicity (back-and-forth) of the wave train.

Among the experiments of Duncan (1981, 1983, 2001), the case with $d/c = 0.783$ has the smallest submergence of the foil and it exhibits a violent complex breaking.

De Blasi et al. (2000) have shown an additional condition, with $d/c = 0.65$. In this case, breaking is violent too, with a complex foamy free surface.

Summarizing, the shape of a wave train generated by a foil underneath the free surface at constant speed is characterized by a pronounced sensitivity to small variations of the incident ambient flow. The wave elevation and the longitudinal position of the zero crossings are generally unsteady, mostly in breaking or quasi-breaking conditions.

Duncan observed the recirculating aerated water of the breaker zone in the attempt to establish the relationships between the geometric parameters of the spilling breaker. Fig. 4 summarizes these parameters.

According to Duncan, the following relationships hold (among others):

a) the relationship between the wavelength λ_b of the breaker and the incident flow speed U in terms of the finite amplitude Stokes wave, reads

$$U = 1.044\sqrt{\frac{g\lambda_b}{2\pi}} \tag{13}$$

b) the breaking region has been observed to have a characteristic oscillation in space and time with an almost regular period T_b approximately equal to 4.4 times the period of a wave with phase speed equal to the hydrofoil speed U, i.e.:

$$T_b = 4.4\frac{\lambda}{U} \tag{14}$$

In this work we focus our attention on the breaking cases only, as shown by Duncan (1983) ($d/c = 0.783$) and by De Blasi et al. (2000) ($d/c = 0.65$), with particular interest to the analysis of the free surface elevation close to the breaker - in terms of averages and amplitude spectrum - and to the effect of the turbulence model on the free surface characteristics.

4.2. Numerical simulations

The numerical simulations shown here refer to 2 different foil depths: 1) $d/c = 0.783$ (case(d) after Duncan (1983)) and 2) $d/c = 0.65$ (after De Blasi et al. (2000)). In the present simulations, the frame of reference is fixed to the foil and $x = 0$ corresponds to the leading edge. The foil depth d is measured from the center point of the chord of the foil.

The Froude number is $Fr = 0.567$ and the Reynolds number is $Re = 1.62 \times 10^5$ (case 1) and $Re = 4.52 \times 10^5$ (case 2) respectively. The angle of attack is $\alpha = 5^\circ$

For the case 2), the onset flow field is derived from the average vertical profile reported in De Blasi et al. (2000). It accounts for the free surface boundary layer induced by the circulating channel. Even with the use of the numerical absorption of waves, there is a relatively strong influence of the domain length on the quality of the results. For this reason and after some tests, the computational domain has been set to $40c$ long downwind and $20c$ long upwind from the leading

edge of the foil. After setting the domain size, in order to avoid reflections from the outer boundary, the useful time window of the simulation has been defined according to the propagation of the wave energy (wave group velocity).

Simulations have been carried out in unsteady mode, with or without turbulence model ($k-\omega SST$ turbulence model of Menter (1994) where the turbulent intensity I and eddy viscosity β are specified at the inlet, respectively $I = 5 \times 10^{-5}$, $\beta = \nu_t/\nu = 2 \times 10^{-2}$). The simulations have been run also with strongly different values of the eddy viscosity, up to $\beta = 10^2$ (not shown here). Within the simulations with turbulence model, no appreciable difference have been observed in terms of free surface profile position and wave amplitude.

The grids used for the computations are composed of 27 structured blocks with $380,000$ cells approx. for the finest grid, with $y^+ \simeq 5$ at the foil surface. Three grids have been prepared for the simulations with increasing number of elements according to a grid refinement factor greater or equal than 1.3 after Celik et al. (2008). The aspect ratio between the size of adjacent cells is never greater than 1.1 according to the best practice and recommendations of ITTC (2014).

The results shown hereafter refer to the finest grid.

4.3. Results and discussion

4.3.1. $d/c = 0.783$ (after Duncan (1983))

Fig. 5 shows the comparison between the experimental profile (empty circles, derived from Fig. 3 (after Duncan) and the time averaged simulated profile (solid thin line with small squares = with turbulence model, solid thick line = without turbulence model). As observed also by Duncan, the wave train exhibits a strong time dependence or quasi-periodicity, with crests and hollows moving sligthly back and forth. Thus the free surface elevation at any longitudinal position has been averaged over a time window that includes an integer number of characteristic periods of oscillation (see discussion below), starting from a condition where the wave train is reasonably fully developed. Fig. 6(a),(b) (left) shows a waterfall of snapshots of the simulated free surface profiles taken at con-

stant time intervals, with turbulence model (a) and without turbulence model (b) respectively. In Fig. 5 the dashed (without turbulence model) and dotted (with turbulence model) lines represent the time averages of the maximum and minimum free surface elevation at each longitudinal position.

Finally Fig. 6(a)(b) (right) shows the amplitude spectrum of the wave elevation at the longitudinal position $x/c = 2$. In both cases (with or without turbulence model), the dominant peak occurs at $\omega_b = 2\pi/T_b = 2.7$ rad/s approx., i.e. 4.4 times the phase speed period, in full agreement with the observations and analytical estimates of Duncan (Eq.(14)).

As expected (Iaccarino et al., 2003), the simulation with a model for turbulence exhibits a smoother behavior of the free surface, both in space and frequency domain (Fig. 6), since this approach acts as a low pass filter for the velocity field. This filtered flow leads to an over-estimation of the first wave crest by a factor 3 approximately (Fig. 5), the scatter of the data around the mean value is rather limited (dotted lines in Fig. 5) and the amplitude spectrum shows a very narrow band (Fig. 6(a) right). On the other hand, without a model for turbulence, the free surface appears scattered around the mean value (dashed lines of Fig. 5) and the amplitude spectrum (Fig. 6(b) right) shows a noisy behavior at frequencies higher than the dominant peak. As shown also in other works in the literature,see for instance (Muscari and Di Mascio, 2004), the wave train profile of the Duncan experiment is hardly well captured by RANS simulations, with a typical strong over-estimate of the first crest and an underestimate of the first hollow, that has been attribuited to an inadequate prediction of the pressure field in the suction zone (Rhee and Stern, 2002).
The presence of breaking takes the flow into a local turbulent regime, with the double consequence of enhancing the air-water mixing at the interface and of switching-on a persistent vorticity field (not shown here).
In the case analyzed, the standard 2-D RANS simulations presented seem to become inadequate in the prediction of averaged free surface elevation; this is probably due to an over-estimation of the eddy viscosity produced by the model (Tian et al., 2012; Zhao et al., 2004; Zhao and Armfield, 2010).

4.3.2. $d/c = 0.65$ *(after De Blasi et al. (2000))*

The results obtained for this test case are shown in Fig. 7 in terms of time averaged wave profile and time averaged maxima and minima around the mean profile. Fig. 8(a)(b) presents the results in terms of waterfall of profiles (left) and amplitude spectrum of the wave elevation at $x/c = 2$ (right). Again the results are shown with (a) or without (b) turbulence model. In this case the inlet vertical velocity profile is derived from the paper of De Blasi et al. (2000).

The conclusions derived in Sec. 4.3.1 still hold or they are even more evident. In this case the wave train shown in the experiments and in the simulation without a model for turbulence is almost totally destroyed by breaking. A thick foamy flow spreads along the wave train. The scatter of the data around the mean value has the same order of magnitude in the simulation and measurements. On the other hand, the simulation with turbulence model shows a smooth breaking wave train, failing completely to predict the first and second wave crests.

The results obtained by the simulations in terms of some parameters of interest in this discussion (wave breaking length and period of horizontal oscillation of the wave crest) are summarized in Table 2. The reference values for the comparison are those computed with Eq.(13) and (14) for $d/c = 0.783$ whereas for the case $d/c = 0.65$ the reference period has been given by De Blasi et al. (2000) directly from the experiments. While the periodicity of the breaking event is captured in both cases $d/c = 0.783$ and $d/c = 0.65$, with or without a model for turbulence, referring to Table 2, the shape of the breaking wave is associated to a larger error when the model for turbulence is adopted. This still occurs even if the grid adopted cannot resolve properly the details of the foamy surface and consequently a lack of accuracy in the simulations without a model for turbulence is expected, at least in that area. This feature is difficult to comment since many elements are expected to contribute and interact. A possible reason can lay in the dependence of free surface solution on the complex pressure field in the suction area.

As concluding remarks for Case I, within the limits of the grid used and of the 2D assumption, the simulations conducted with a standard RANS approach show weakness in reproducing some features of the awaited breaking events. The reasons for this difficulty probably combine together. Following Rhee and Stern (2002), the first hollow position may be difficult to catch because related to the accuracy in the prediction of the pressure field; the same reason could have a role in the prediction of breaking wave asymmetry (λ_b), while the wave crest, higher then expected, could be associated to the fact that turbulence production and dissipation occurs in different parts of the traveling wave, indicating that in these regions the assumption of equilibrium requested in the RANS approach is not correct (Zhao et al., 2004). Furthermore, the transition from laminar to turbulent regime may play a role too and its onset is not accounted for by a standard RANS approach. Viceversa, the same RANS approach captures the quasi-periodic breaking occurrence T_b as clearly evidenced by the spectral analysis of the free surface elevation. In this case the relatively low frequency is far from those filtered in the turbulence model (Iaccarino et al., 2003).

5. Case II: ultra-shallow water cnoidal waves breaking in spilling and plunging mode on a sloping beach

5.1. Problem formulation

Cnoidal waves are surface gravity waves of fairly long wavelength when compared with water depth. They represent the solution of the Kortweg and deVries equation and in the limit of infinite wavelength, the cnoidal wave becomes a solitary wave. From the mathematical point of view, the complete solution has been given in terms of rational numbers (Fenton, 1998). We refer to this work in the following definitions. Surface elevation and fluid velocity has been defined in terms of cnoidal function cn, the ratio of wave height to trough, depth and the elliptic parameter m. When $m < 0.96$, a 3^{rd} order representation for relatively short and not so high waves becomes feasible, while the 5^{th} order representation is preferred when the m parameter is very close to 1.

A relevant dimensionless parameter is the Ursell number U_r, where:

$$U_r = \frac{H}{h}(\frac{\lambda}{h})^2 \tag{15}$$

U_r determines a wave in terms of ratio between non linearity (as the ratio between wave height and water depth) and shallowness (as the squared ratio between wave length and water depth). In case of waves with $U_r < 5$ the linear theory is adequate, then a zone in between Stokes theory and cnoidal theory lays in the range of $10 < U_r < 25$. According to other evidences, cnoidal theory should be applied for $U_r > 40$, while for lower values, Stokes theory could be used (Hedges, 1995).

In this work the numerical study is concerned with the reproduction of shallow water waves propagating initially in a constant depth and then breaking on a sloping beach (ramp).

Reference is made to the experiments of Ting and Kirby (1994), Ting and Kirby (1995), Ting and Kirby (1996) and to the numerical simulations of Xie (2013). The attention is here focused on the capability of the simulation to reproduce two types of breakers, spilling and plunging respectively. The key point regards the shape of the wave profile at breaking, in both spilling and plunging conditions, and the position of the breaker along the ramp.

5.2. Numerical simulations

Referring to the experiments in Ting and Kirby (1994, 1995, 1996) and to the numerical simulations in Xie (2013) and in Chella et al. (2015), the computational domain here used is sketched in Fig. 9 with the relevant symbols. The left boundary acts as a wavemaker where the cnoidal wave model of Fenton (1998) is applied in order to reproduce the waves with parameters given in Table 3. They propagate initially in a constant depth of 0.4 m with a wavelength of 3.70 and 10.76 m for the spilling and plunging breaker respectively. Afterwards the wave train reaches a 1/35 slope ramp where waves are supposed to break at a specific position x_b.

The goals of this section of the paper are:

a) to reproduce spilling and plunging breaker shapes with a wavemaking inlet boundary condition consistent with the cnoidal wave theory;

b) to capture the correct breaking position x_b of the waves along the ramp;

c) to compare the surface elevation with experimental results at different stations along the domain/ramp;

d) to see the effect of turbulence model on the breaker characteristics.

The initial conditions consist of an unperturbed flat free surface. A zero normal derivative for the pressure is prescribed at the inlet. A constant total pressure is assigned at the top boundary and a blended zero gradient and fixed value condition is specified for the velocity field.

Simulations have been carried on with the $k-\omega SST$ turbulence model of Menter (1994) where the turbulent intensity I and eddy viscosity β are specified at the inlet, $I = 2.5 \times 10^{-3}$ and eddy viscosity $\beta = \nu_t/\nu = 0.1$.

The grids used for the computation are composed of 7 structured blocks with a maximum of $900,000$ cells approx (finest grid). The first grid cell at the bottom boundary layer has a thickness of 0.002 m (after the previous study of Chella et al. (2015).) Three grids have been prepared for the simulations with increasing number of elements according to a grid refinement factor greater or equal than 1.3 after Celik et al. (2008). The aspect ratio between the size of adjacent cells is never greater than 1.1 according to the best practice and recommendations of ITTC (2014).

The results shown hereafter refer to the finest grid.

5.3. Results and discussion

A sequence of snapshots of the simulated spilling and plunging breakers is reported in Fig. 10(a-e) and Fig. 11(a-e) respectively, as obtained with a RANS approach. The time step between the snapshots is $T/20$ and $T/10$ respectively. The contour variable is the volume fraction α. The capability of the model to capture position of the breaker (x_b) accurately is among the crucial aspects of this kind of simulations. The experimental position of x_b, as given in Ting and Kirby (1994), Ting and Kirby (1995) and Ting and Kirby (1996) (approximate

assumption of incipient breaking, i.e. the wave profile starts being a multivalued curve), is evidenced with a solid vertical line.

Fig. 10(a-e) shows a sequence of snapshots of the volume fraction of a single breaking event among those simulated. The data are obtained within the standard RANS approach. The incipient breaking occurs in a slight advance with respect to experimental measurement (a). The spilling breaker appears initially as a "small" size spilling phase followed by a jet of liquid ejected from the wave crest (b). This initial jet is expected to hit the front of the wave, close to the crest, starting to entrap foam. In the meanwhile the wave moves forward and, depending on the velocity field near the free surface, a roller where air and bubbles are mixed together may take place (c), (d) and (e). This mechanism is qualitatively reproduced in our simulations, consistently with the grid resolution.

In the plunging breaker case, Fig. 11(a-e), the simulation anticipates the breaking position x_b on the ramp by a distance of approximately 5% of the undisturbed wave length, but still the agreement is rather satisfactory.

Compared with spilling breakers, plunging breakers have the ability to entrain a bigger quantity of air and at greater depths, with larger bubbles entrapped in the water column. This is described as an important mechanism since it relates to dissipation. With reference to Fig. 11(a-e), obtained with a standard RANS approach, a discontinuous overturning jet is observed to move from the wave crest. In (a) and (b), the onset of the breaking appears slightly anticipate in comparison with the experimental measurement (black line). After the impingement, the air cavity entrapped by the overturning jet is then observed to break up into bubbles of different sizes (c), (d) and (e).

The size of the jet originally generated at the wave crest is important since it relates to the onset of the plunging mechanism. In particular, an insufficient resolution (Lubin et al., 2011) in space or the schemes in use for the divergence terms in the VOF equations (Chen et al., 2011) can lead to unfeasible impingement with the consequence of a wrong physics prediction. For these reasons, this topic has been considered, for instance, by Lubin et al. (2006) within the

framework of 3D Large Eddy Simulations. In our case it was not possible to evince details on the jet size from the paper of Ting and Kirby (1995), and for this reason, in our models we tried to overcome this problem by ensuring a grid resolution similar to that of recent literature (Chella et al., 2015) and using upwind schemes only for turbulent quantities.

A comparison between experimental and numerical results regards the time traces of the surface elevation at different stations along the direction of propagation. Accordingly to the available experimental data, in the spilling breaker case (Fig. 12), the positions of the gauges are at $x = -1.5, -0.5, 4.5, 5.5, 6.0, 6.5, 7.0, 8.0$ m (Ting and Kirby (1996) as reported in Chella et al. (2015)), in the plunging breaker case (Fig. 13), the positions of the gauges are at $x = -1.5, 2, 4, 6, 8, 9, 10, 11$ m (Ting and Kirby, 1996). In both cases, the time traces show five periods of the simulations in almost stabilized breaking conditions. The agreement is again rather satisfactory, in terms of wave elevation and phase lag at each station of both type of breakers and in line with the results of other investigators (Chella et al., 2015; Xie, 2013).

Fig. 10 and Fig. 11 have been previously shown to witness qualitatively the breaking mechanism captured by the numerics (air entrainment, jet impingement). Fig. 12 and Fig. 13 show a a direct comparison with experimental measurements and the numerical results of other investigators that recently approached the same problem with a comparable grid resolution and numerical approach (Chella et al., 2015). Differently from Case I, the RANS simulations reasonably reproduce the wave breaking while the results of the simulations without turbulence model show a large advance in the breaking position along the ramp and consequently a corrupted wave propagates along the rest of the ramp, both in spilling and plunging case; this is probably due to a larger amount of foam and air entrapped that grid and time resolution could not account for. A further step in the analysis is finally consistent with the RANS approach and accounts for phase averages.

Fig. 14 shows the comparison between experimental Ting and Kirby (1996) and present numerical results (with turbulence model) for the spilling breaker case.

The phase-averaged time traces of the surface elevation along the ramp are given for the positions (a) $x = 7.275$m, (b) 7.885m, (c) 8.495m, (d) 9.110m after Ting and Kirby (1996). In particular the surface elevation parameter is $\frac{\zeta-\bar{\zeta}}{h}$, where $\bar{\zeta}$ is the phase averaged elevation at the generic station x and h is the water depth at the same station x. Both experimental and numerical peak values over the considered period decrease with increasing x, or in non-dimensional form with increasing $(x-x_b)/h_b$, where h_b is the water depth at breaking. Considering the complexity of the physical phenomenon and the rough treatment of turbulence at breaking with a RANS model, the agreement can be considered satisfactory for the purposes of this work.

Finally, Fig. 15 shows a further comparison between experimental Ting and Kirby (1995) and present numerical results (with turbulence model) for the plunging breaker case. The phase-averaged time traces of the surface elevation along the ramp are given in non-dimensional form for the positions (a) $x = 7.795$m, (b) 8.345m, (c) 8.975m, (d) 9.295m. As shown in Fig. 11, in our simulations we find a slightly premature breaking along the ramp. Thus at the positions (a) to (d), the crest height is underestimating systematically the experimental values. On the other hand we observe that our results are in line with those shown in Zhao et al. (2004) and obtained with a standard Reynolds stress model. In the same paper, tha authors have shown better results obtained with a $k-l$ model in which the artificial energy cascade process is introduced explicitly by a model suited for a 2D flow.

The research conducted on this specific topic has involved many investigators (Zhao et al. (2004), Zhao and Armfield (2010), Kimmoun and Branger (2007)) showing that the more accurate and expensive techniques (in terms of grid resolution and advanced numerical frameworks) have been capable to give the most accurate prediction of the various aspects concerning the breaking, specifically the free surface elevation and the velocity profiles (Lubin et al. (2006), Lubin et al. (2011), Chella et al. (2015), Christensen (2006)).

6. Case III: breaking of regular waves induced by a weakly submerged horizontal cylinder at a low Keulegan-Carpenter number

6.1. Problem formulation

In this section, we investigate the breaking of regular waves induced by a weakly submerged horizontal cylinder with axis perpendicular to the direction of propagation of the waves. The incident wavy flow is characterized by a very low Keulegan Carpenter number, $KC = 0.8$.

Fig. 16 shows a sketch of the physical problem and relevant symbols. Here a is the radius of the cylinder, $D = 2a$ its diameter, λ is the incident wave lenght, H is the incident wave height, T is the incident wave period, h is the water depth.

The Reynolds ($Re = \frac{\rho U_{ref} D}{\mu}$) and Keulegan Carpenter ($KC = \frac{U_{ref} T}{D}$) numbers are computed in relation to the incident (unperturbed) wave kinematics computed conventionally at the cylinder axis. Stokes 3^{rd} order wave theory is used to compute the reference velocity U_{ref}.

The problem has been studied by several authors, both experimentally and numerically (see Contento and Codiglia (2001) for a brief review). Among others Chaplin (1984a,b, 1992, 1993) and Contento and Codiglia (2001) have shown experimentally the strong nonlinear behavior of the inertia (pressure) forces acting on the cylinder, as a result of a steady streaming (of viscous origin) around the cylinder surface, induced by the orbital nature of the incident flow.

For such low KC numbers (< 3), the inertia forces are expected to be the only contribution to the wave load and the inertia coefficient C_m of the Morison equation, Eq.(16), is expected to be ≈ 2.

$$F(t) = C_m \rho \frac{\pi D^2}{4} \frac{dU}{dt} + \frac{1}{2} C_d \rho D U |U| \tag{16}$$

where $F(t)$ is the force per unit length of the cylinder. Unexpectedly, due to this orbital streaming that induces a kind of Magnus effect in anti-phase with the inertia force, C_m drops down well below 1 at $KC \approx 2.5$ as $A - B \cdot KC^2$, the values of A and B being basically a function of the submergence of the cylinder.

Another strong nonlinear effect evidenced by the experiments (Contento and Codiglia, 2001) regards the higher order contributions that arise in both the pressure field on the cylinder wall related forces (Chaplin (1984a,b, 1992, 1993)) and on the free surface elevation, the magnitude of these higher order terms being again a function of the submergence of the cylinder and of the KC number.

These considerations describe some of the physiscal aspets of the problem that has been studied experimentally at the wave basin of the University of Trieste (Contento and Codiglia, 2001), showing, at the lowest submergence of the cylinder, a wave gently breaking above the cylinder. For this reason it has been selected as third case of this work.

6.2. Numerical simulations

The cylinder diameter is $D = 2a = 0.315$ m, the depth of the cylinder axis is $y/a = -2$, the incident wave length is $\lambda = 4$m, the wave height $H = 0.1273$m, the water depth is $d = 1.55$m, $KC = 0.8$, $Re = 43372$ and the diffraction parameter is $ka = 0.2474$, where k is the wave number. Table 4 summarizes the design parameters of the simulation.

Similarly to what has been done in the physical lab, the incident waves have been simulated separately (without the cylinder), with the same domain size and resolution at the free surface. In this way it has been possible to obtain the exact phase lag between the unperturbed incident flow and the free surface and pressure perturbed by the presence of the cylinder.

Hereafter we assume time $t = 0$ at the zero crossing-up of the unperturbed incident wave elevation at the longitudinal position of the cylinder axis.

The computational domain used is set into a block structure that allows a straightforward refinement in the near wall region ($O - grid$) and at the free surface interface (here with a constant vertical spacing). The domain is assumed to be 26m long downwind and 18m long upwind, with respect to the cylinder axis position.

Waves are generated at the left boundary of the domain. The target steepness of the incident waves is less than 1/30 so that the linear wave kinematics

can be applied as boundary condition at the wave-making patch with an acceptable approximation. Due to the finite amplitude elevation of the free surface, the velocities at the wavemaking boundary have been modified (not shown here) in order to fulfill both a zero net flux during a complete wave period and consistent velocity values above the mean free surface. A sponge layer extending 2 wavelengths has been adopted here (see Sec. 3).

Due to the very low nominal Reynolds number, the simulations presented here have been carried out with and without the turbulence model. In the former case the turbulent intensity I and eddy viscosity β are specified at the inlet as follows, $I = 1.0 \times 10^{-2}$ and $\beta = \nu_t/\nu = 10^{-1}$.

In this case the grid has been prepared with 3×10^6 points and 28 blocks, with $y^+ \simeq 1$ at the cylinder wall. The aspect ratio beteween the size of adjacent cells is never greater than 1.05 in order to ensure the best sampling of the wave fields in space.

6.3. Results and discussion

As an instrument for the analysis of the results, the phase averages of free surface and dynamic pressure at the cylinder surface have been presented and compared with experimental results. In this case, numerical results from other authors have not been found in literature. Fig. 17 to Fig. 24 show a sequence of snapshots of the free surface elevation and pressure at the cylinder wall, equally spaced in time t according to $t/T = j/8$, with $j = 0, 1, 2 \ldots 7$ where T is the incident wave period. As stated before, time t is assumed to be zero at the zero crossing-up of the unperturbed incident wave elevation at the cylinder axis. The dotted line represents the incident wave profile (simulated separately); the solid lines represent the free surface and the dynamic pressure without turbulence model. A positive dynamic pressure is plotted outside the cylinder surface,negative is inside the cylinder. The dashed lines represent the free surface and the dynamic pressure with turbulence model switched-on. On the same plot the solid rhombus represents the experimental elevation of the unperturbed wave at the cylinder axis. Finally the empty circles represent the free

surface and pressure measurements after Contento and Codiglia (2001). The mean uncertainty level of the measured wave elevation and dynamic pressure is ± 0.0015 m and ± 0.01 kPa respectively for the Bias error, and approximately ± 0.002m and ± 0.1 kPa for the RMS. These RMS values are due mainly to the fluctuation of the signal within consecutive periods. Thus both measured and simulated values in the plots represent average values computed over four time instants t evenly spaced in time, $t = t_0 + i \cdot T$ for any i. The time window corresponds to a quasi-stationary part of the Fourier components of the signal. The agreement of both pressure and free surface elevation is excellent at each t/T. The influence on the pressure distribution of the shallow water condition above the cylinder and of the wave breaking is reproduced extremely well, as shown in Fig. 17 and Fig. 24 for $t/T = 0/8$ and $t/T = 7/8$ respectively.

As a whole, the simulations with turbulence model show a rather good agreement, even though there is a systematic underestimation of the dynamic pressure and a smoother behavior of the free surface elevation at the breaker. It is really difficult to identify an unique reason for this. Certainly, free surface elevation and dynamic pressure at the cylinder have been observed to be strictly connected during all the phases of the averaged wave period analyzed and it is possible that the RANS approach lacks of the accuracy in the prediction of the free surface since the same happens for the prediction of the vortices detached from the cylinder surface, being this occurrence non-steady and related to a local adverse pressure gradient that is hard to capture on curved surfaces invested by wavy flows (Menter, 1994).

The presence of rotating structures detaching from the cylinder surface is represented in Fig. 25(a)(b) that shows a contour plot of the non-dimensional vorticity $\omega^* = \frac{\omega}{U/D}$ for $t/T = 9/80$ and $15/80$ respectively. The complexity of the flow field in terms of detached large eddies at the cylinder surface and of eddy riding at the breaker is well evidenced (Lupieri and Contento, 2015). The volume fraction (not shown) at breaking exhibits a pronounced mixture of air-water over a thick layer at the interface.

As discussed in Sec. 6.1, Chaplin (1984a,b, 1992, 1993) and Chaplin and

Ikeda (1999) have shown experimentally that the interaction at low KC numbers of a 2D regular wave train with a weakly submerged cylinder with axis parallel to the wave crests leads to a pronounced steady streaming in the boundary layer. This effect has viscous origins and is responsible of the large drop of the inertia (pressure) force. The experimental data of Contento and Codiglia (2001) have shown that, keeping KC constant while varying the submergence of the cylinder, the higher order Fourier components of the Morison's force (Eq.(16)) and of the flow (pressure), exhibit a strongly nonlinear dependence on the submergence of the body, the deeper the cylinder is, the lower the amplitudes of the second and third harmonic are (Lupieri and Contento, 2015). Fig. 26 shows the clockwise averaged velocity field around the cylinder surface. The time window used for computing the average vectors is the same as reported above (4 consecutive complete wave periods).

7. Conclusions

This work has focused the attention on the numerical reproduction of 2-D wave breaking events as propaedeutic benchmark for more complex 3D situations, like the resistance of a ship in calm water including breaking or the loads of large breaking waves on a fixed or moving structure.

The cases investigated by means of numerical simulations are quasi-steady breaking induced by a fully submerged hydrofoil at constant speed in calm water, ultra shallow water cnoidal waves breaking in spilling and plunging mode on a sloping beach and breaking of intermediate water depth regular waves induced by a weakly submerged horizontal cylinder at a low Keulegan-Carpenter number. The experimental cases examined belong to nominally laminar or transient regime. However either the gentle breaking or the violent splashing produce a mixing of air and water at the free surface interface and this leads the flow to a local turbulent regime.

In the case of the submerged hydrofoil, the simulation with turbulence model shows a smooth breaking wave train, but it fails completely to predict the first

and second wave crests, both in longitudinal position and mostly in breaker height. The simulation without turbulence model, probably under-resolved in space, shows a thick foamy flow that spreads along the wave train, as evidenced in the experiments too. In this case the scatter of the data around the mean value has the same order of magnitude for both simulations and measurements. The low frequency periodicity of the wave elevation (predicted by the theory and shown with non-negligible difficulties by the experiments) appears clearly when the turbulence model is used, due to its implicit low-pass filtering (Iaccarino et al., 2003).

The breaking of cnoidal waves in spilling and plunging mode, traveling on a ramp has been simulated with satisfactory results. It is shown that the simulated surface elevation is very close to the experimental data, with just a slight difference in the detection of the breaking position and peak values.

In the case of the circular cylinder in regular waves, the free surface elevation and the pressure at the cylinder wall are in very close agreement with the experimental data.

Summarizing, the results obtained in this work using a standard turbulence model are in a general good agreement with both experiments and other numerical solutions from the literature. The worse case obtained regards the wave train generated by a foil at steady speed, irrespective of grid resolution and interface-capturing method (Contento et al., 2015). On the other hand, in the case of bottom induced breaking, the grid resolution has been shown to play a key role in the reproduction of the position and mostly of the local features of the breaker.

In any case, as shown also by the wide literature, there are undeniable difficulties in simulating very accurately breaking waves with a standard RANS approach. For the three cases here considered, the reasons have been widely discussed, with support from the literature, leading to consider alternative ways to take turbulence into account at breaking, but still in a RANS context. For instance, the high level of eddy viscosity produced by the adopted turbulence model in the breaking region could be limited with a different formulation of

the turbulence production term, as sometimes practiced in external aerodynamics for fluxes with high level of streamlines curvature. A radically different approach could be Large Eddy Simulations or the promising DES technique, as already shown in the literature for one of the selected cases (Christensen, 2006). However, even with 3D LES and even with the adoption of different sub-grid models, Christensen (2006) has shown that the position of breaking is still shifted from the experimental one, (slightly) forth or back for spilling or plunging breakers respectively.

8. Acknowledgements

The ERDF - European Regional Development Fund - Friuli Venezia Giulia Region Operational Program POR FESR 2007-2013 and the "Programma Attuativo Regionale del Fondo per lo Sviluppo e la Coesione (PAR FSC) 2007-2013 - Linea d'Azione 3.1.2" are acknowledged for providing the financial support of the OpenSHIP and Open*View*SHIP Projects respectively.

9. Tables

	Term	Discretization
Gradient	∇	linear
	$\nabla \cdot (\rho\phi U)$	limited linearV 1
Convection	$\nabla \cdot (\phi\alpha)$	vanLeer
	$\nabla \cdot (\phi_{rb}\alpha)$	interfaceCompression
Laplacian	∇^2	linear corrected

Table 1: Numerical schemes in use in the simulations.

	$d/c = 0.783$ (SST)	$d/c = 0.783$	$d/c = 0.65$ (SST)	$d/c = 0.65$
Error (%) λ_b	9	3	26	7
Error (%) T_b	9	9	12	12

Table 2: Errors in the breaker parameters of the simulated waves according to the results of Duncan (1983) and De Blasi et al. (2000) - Case I.

	λ(m)	H(m)	T(s)	h(m)	m	U_r	Order	x_b(m)
Spilling	3.70	0.125	2.0	0.40	0.87	27.97	3^{rd}	6.40
Plunging	10.76	0.128	5.0	0.40	0.99	230	5^{th}	7.79

Table 3: Parameters of the cnoidal waves simulated - Case II.

D(m)	λ(m)	H(m)	T(s)	KC	Re	ka	y/a
0.315	4	0.1273	1.6009	0.80	43372	0.2474	-2

Table 4: Parameters of the simulation of wave breaking over a circular cylinder - Case III.

10. List of figures caption

Figure 1. Schematic representation of a computational domain with wave absorbing zone.

Figure 2. Waves induced by a foil towed underneath the free surface: schematic representation.

Figure 3. Wave profiles induced by a NACA0012 foil at $U = 0.80$ m/s in fresh water after Duncan (1983).

Figure 4. Spilling breaker parameters (after Duncan (1981).

Figure 5. Comparison between the simulated and experimental wave profile: empty circles = experiments after Duncan (1983); thin solid line with squares= time averaged free surface profile from the simulation with turbulence model; dotted lines = time averaged max and min free surface profile from the simulation with turbulence model; thick solid line= time averaged free surface profile from the simulation without turbulence model; dashed lines = time averaged max and min free surface profile from the simulation without turbulence model ($d/c = 0.783$).

Figure 6. Waterfall of snapshots of the free surface profile (left) and amplitude spectrum (right) of the wave elevation at $x/c = 2$: a) = with turbulence model, b) = without turbulence model ($d/c = 0.783$).

Figure 7. Comparison between the simulated and experimental wave profile: empty circles = experiments after De Blasi et al. (2000) (mean +/- RMS); thin solid line with squares= time averaged free surface profile from the simulation with turbulence model; dotted lines = time averaged max and min free surface profile from the simulation with turbulence model; thick solid line= time averaged free surface profile from the simulation without turbulence model and with numerical uncertainty bars; dashed lines = time averaged max and min

free surface profile from the simulation without turbulence model ($d/c = 0.65$).

Figure 8. Waterfall of snapshots of the free surface profile (left) and amplitude spectrum (right) of the wave elevation at $x/c = 2$: a) = with turbulence model, b) = without turbulence model ($d/c = 0.65$).

Figure 9. Wave breaking on a sloping beach: schematic representation.

Figure 10. Spilling breaker on a 1 : 35 ramp. The contour variable is the volume fraction. The time step between the snapshots is $T/20$. The vertical line shows the position $x_b = 6.40$ m of expected breaking, according to the measurements of Ting and Kirby (1994, 1996).

Figure 11. Plunging breaker on a 1 : 35 ramp. The contour variable is the volume fraction. The time step between the snapshots is $T/10$. The vertical line shows the position $x_b = 7.79$ m of expected breaking, according to the measurements of Ting and Kirby (1994, 1996).

Figure 12. Spilling breaker on a 1 : 35 ramp. Comparison between experimental (Ting and Kirby (1996) as reported in Chella et al. (2015)), numerical results from Chella et al. (2015) and present numerical results. Free surface elevation at 8 gauges along the ramp. $x = -1.5, -0.5, 4.5, 5.5, 6.0, 6.5, 7.0, 8.0$ m (top-down); empty circles = experiments; thick solid line with squares= free surface profile from the present simulation with turbulence model; thin solid line= free surface profile from the present simulation without turbulence model, dashed line = results from Chella et al. (2015).

Figure 13. Plunging breaker on a 1 : 35 ramp. Comparison between experimental (Ting and Kirby (1996) as reported in Xie (2013)) and present numerical results. Free surface elevation at 8 gauges along the ramp. x = -1.5, 2, 4, 6, 8, 9, 10, 11 m (top-down); empty circles = experiments; thick solid line with squares= free surface profile from the present simulation with turbulence model; thin solid line= free surface profile from the present simulation without turbulence model.

Figure 14. Spilling breaker on a 1 : 35 ramp. Comparison between experimental (Ting and Kirby, 1996) and present numerical results. Free surface elevation at 4 gauges along the ramp. $(x - x_b)/h_b = 4.397$ (a), 7.462 (b),

10.528 (c), 13.618 (d); empty circles = experiments; solid line with squares= free surface profile from the simulation with turbulence model.

Figure 16. Regular wave breaking over a submerged circular cylinder: schematic representation.

Figure 17. $t/T = 0/8$.

Figure 18. $t/T = 1/8$.

Figure 19. $t/T = 2/8$.

Figure 20. $t/T = 3/8$.

Figure 21. $t/T = 4/8$.

Figure 22. $t/T = 5/8$.

Figure 23. $t/T = 6/8$.

Figure 24. $t/T = 7/8$. Wave elevations at $t/T = j/8$, with $j = 0, 1, 2, \ldots 7$. Dotted line = incident wave profile (simulated separately); thick solid line = free surface elevation and dynamic pressure without turbulence model, dashed line = free surface elevation and dynamic pressure with turbulence model; solid rhombus = experimental (undisturbed) wave elevation at the cylinder axis, empty circles = free surface elevation and dynamic pressure measurements (Contento and Codiglia, 2001).

Figure 25. Contour plot of non-dimensional vorticity at $t/T = 9/80$ (without turbulence model) on (a) and at $t/T = 15/80$ on (b).

Figure 26. Velocity field close to the cylinder surface, averaged over 4 complete incident wave periods. The reference velocity U_{ref} corresponds to the velocity used to define di KC number.

11. Figures

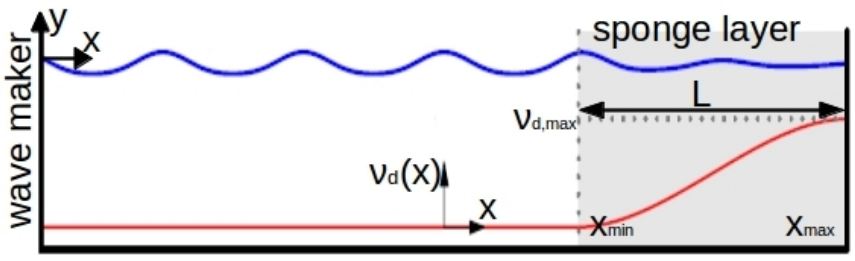

Figure 1: Schematic representation of a computational domain with wave absorbing zone.

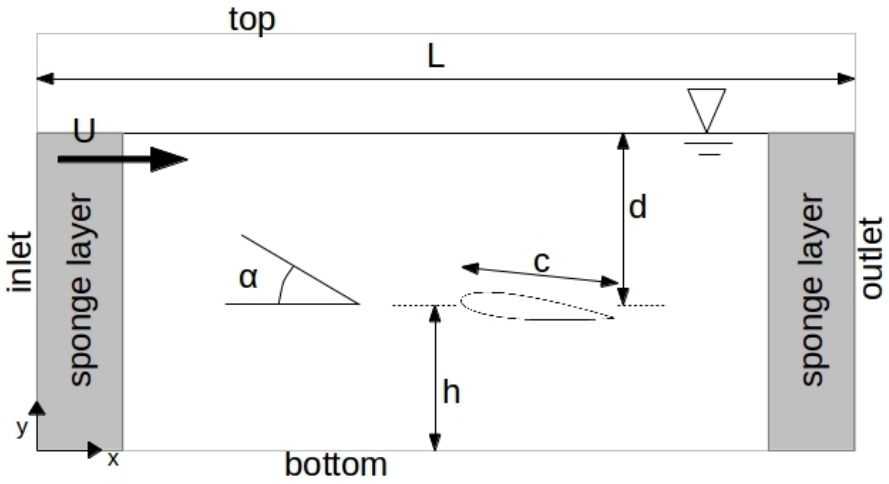

Figure 2: Waves induced by a foil towed underneath the free surface: schematic representation.

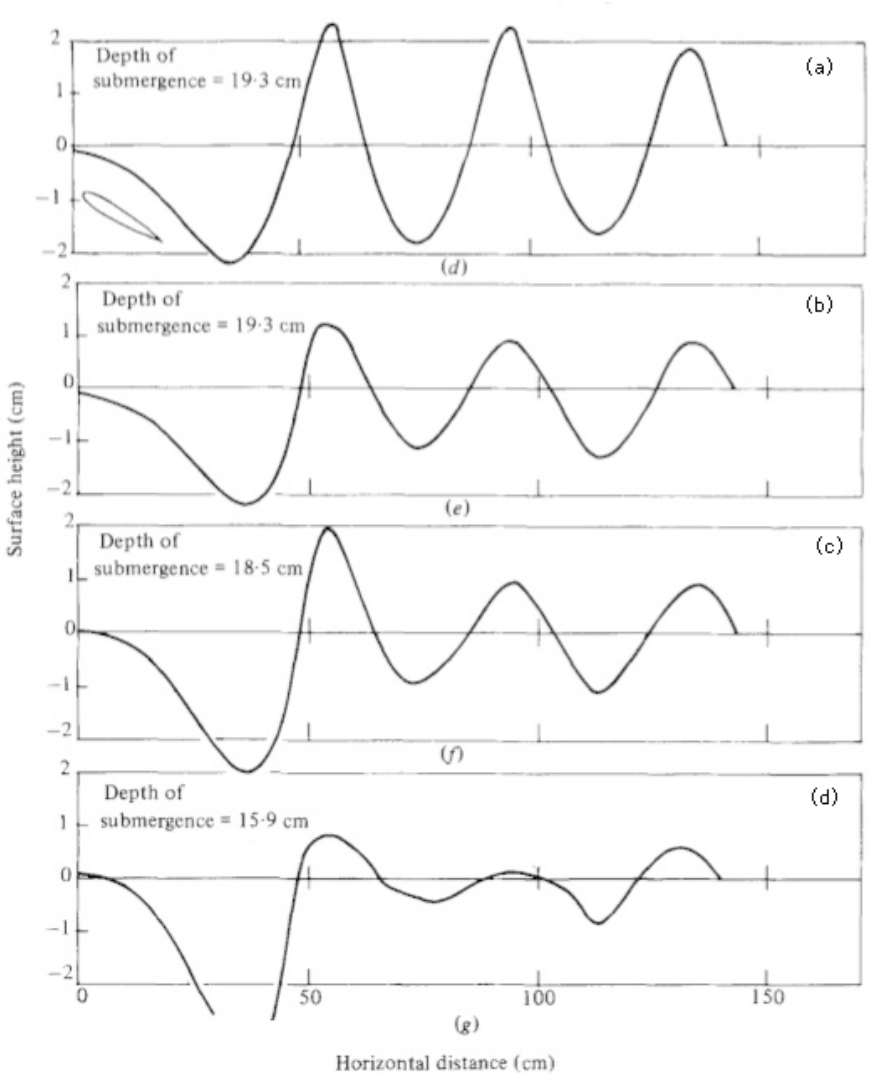

Figure 3: Wave profiles induced by a NACA0012 foil at $U = 0.80$ m/s in fresh water after Duncan (1983).

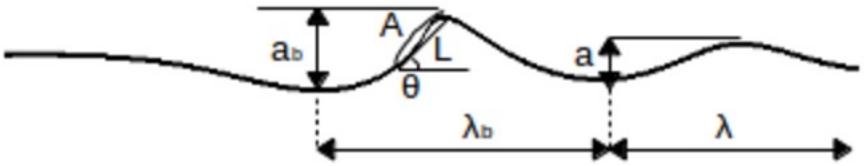

Figure 4: Spilling breaker parameters (after Duncan (1981).

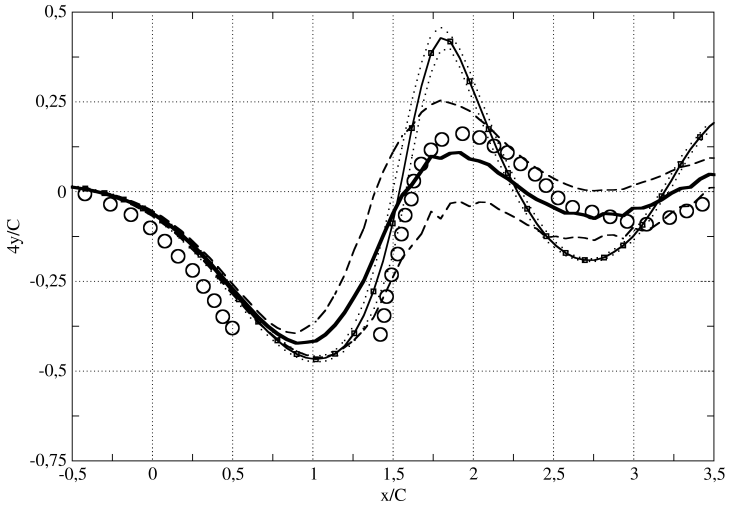

Figure 5: Comparison between the simulated and experimental wave profile: empty circles = experiments after Duncan (1983); thin solid line with squares= time averaged free surface profile from the simulation with turbulence model; dotted lines = time averaged max and min free surface profile from the simulation with turbulence model; thick solid line= time averaged free surface profile from the simulation without turbulence model; dashed lines = time averaged max and min free surface profile from the simulation without turbulence model ($d/c = 0.783$).

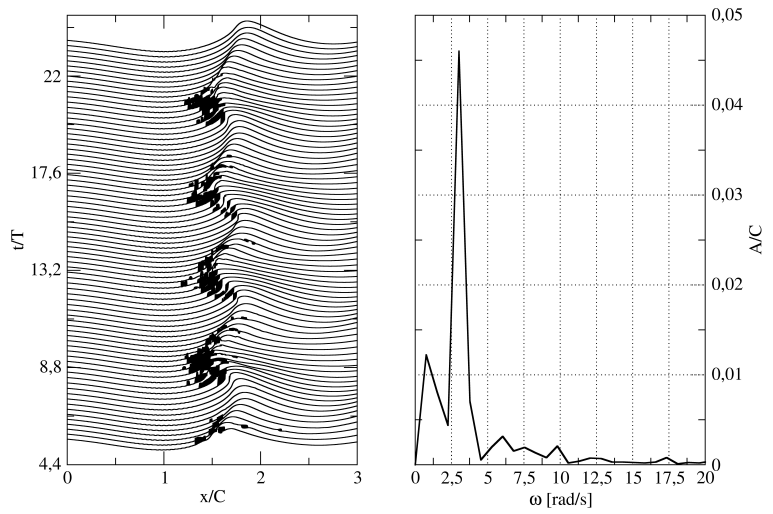

(a)

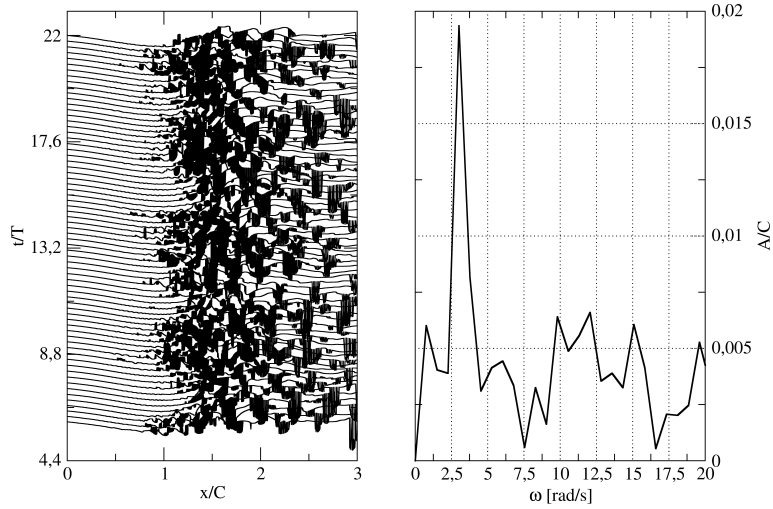

(b)

Figure 6: Waterfall of snapshots of the free surface profile (left) and amplitude spectrum (right) of the wave elevation at $x/c = 2$: a) with turbulence model, b) = without turbulence model ($d/c = 0.783$).

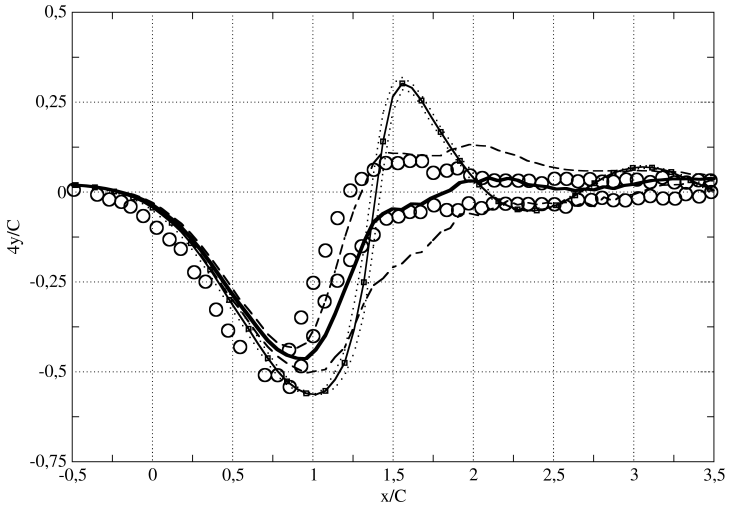

Figure 7: Comparison between the simulated and experimental wave profile: empty circles = experiments after De Blasi et al. (2000) (mean +/- RMS); thin solid line with squares= time averaged free surface profile from the simulation with turbulence model; dotted lines = time averaged max and min free surface profile from the simulation with turbulence model; thick solid line= time averaged free surface profile from the simulation without turbulence model and with numerical uncertainty bars; dashed lines = time averaged max and min free surface profile from the simulation without turbulence model ($d/c = 0.65$).

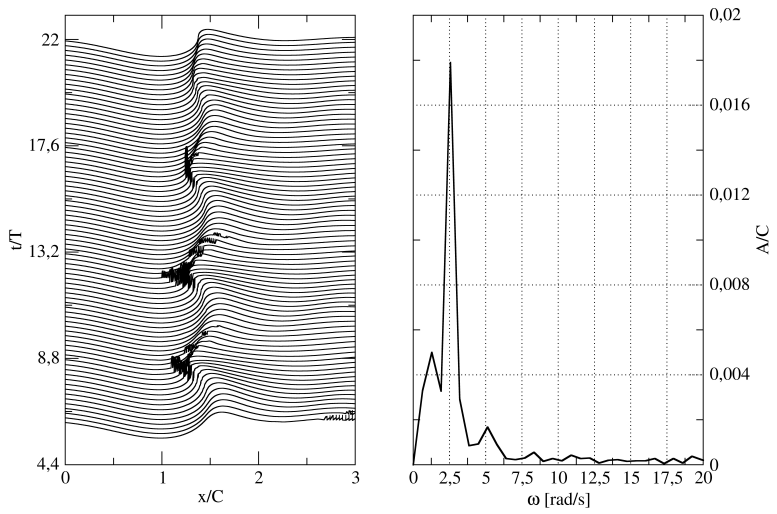

(a)

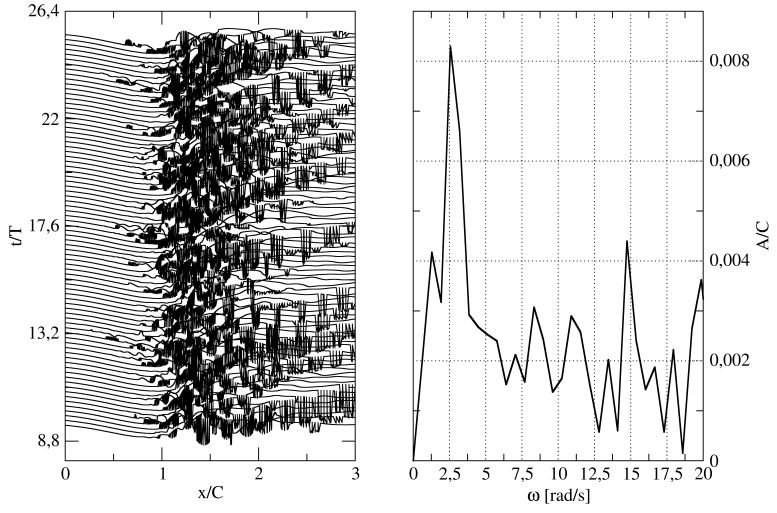

(b)

Figure 8: Waterfall of snapshots of the free surface profile (left) and amplitude spectrum (right) of the wave elevation at $x/c = 2$: a) with turbulence model, b) = without turbulence model ($d/c = 0.65$).

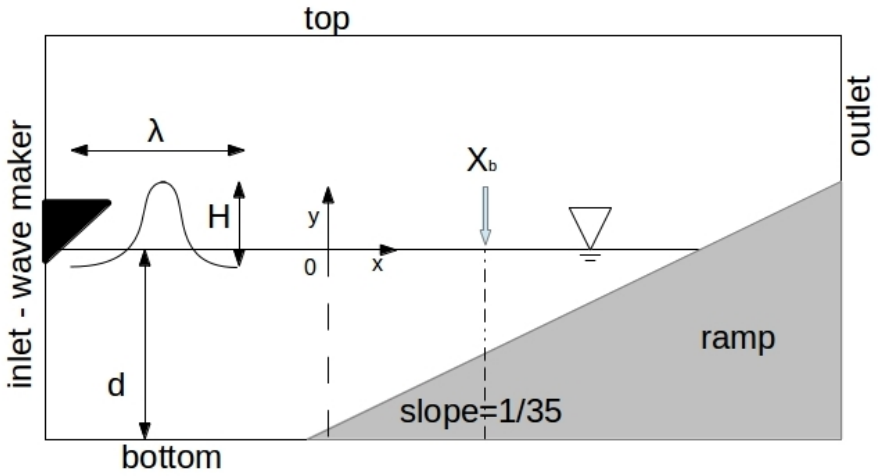

Figure 9: Wave breaking on a sloping beach: schematic representation.

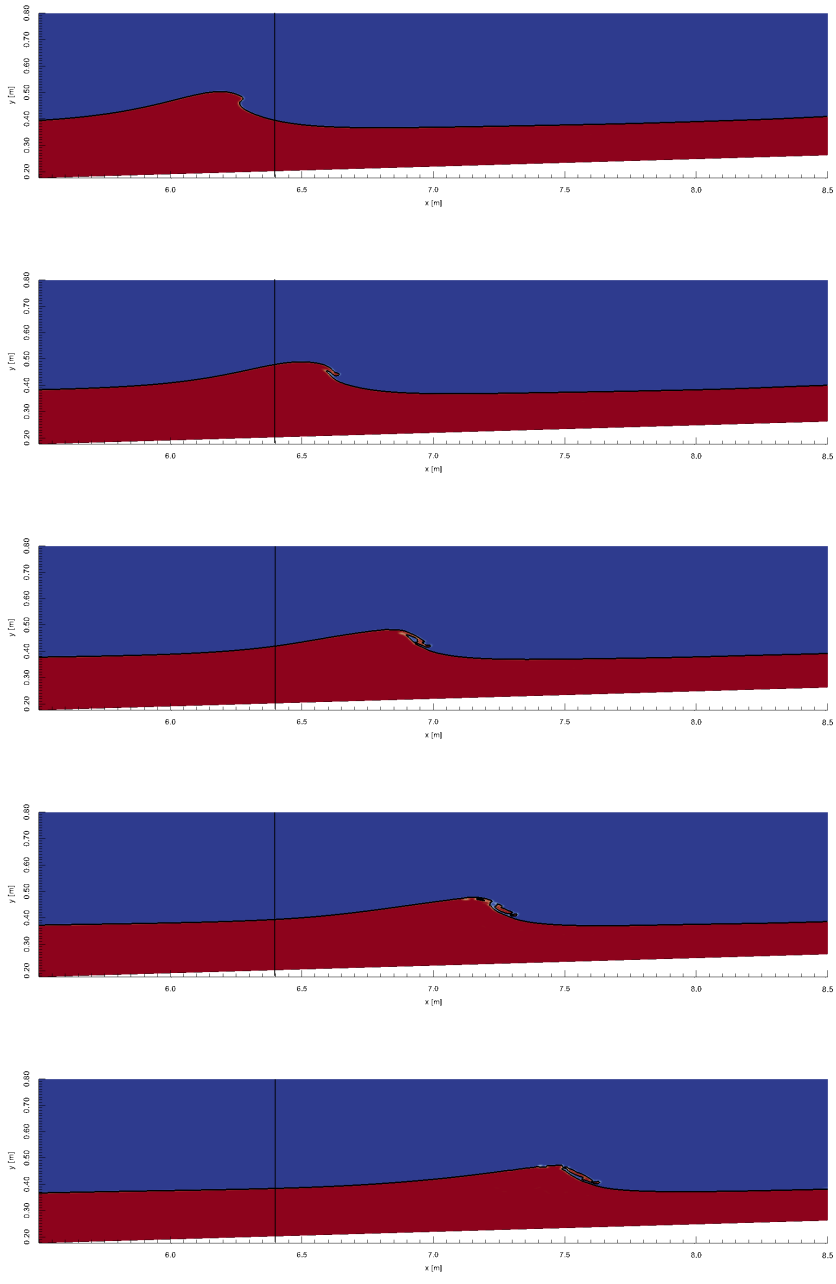

(a) (b) (c) (d) (e)

Figure 10: Spilling breaker on a 1 : 35 ramp. The contour variable is the volume fraction. The time step between the snapshots is $T/20$. The vertical line shows the position $x_b = 6.40$m of expected breaking, according to the measurements of Ting and Kirby (1994, 1996).

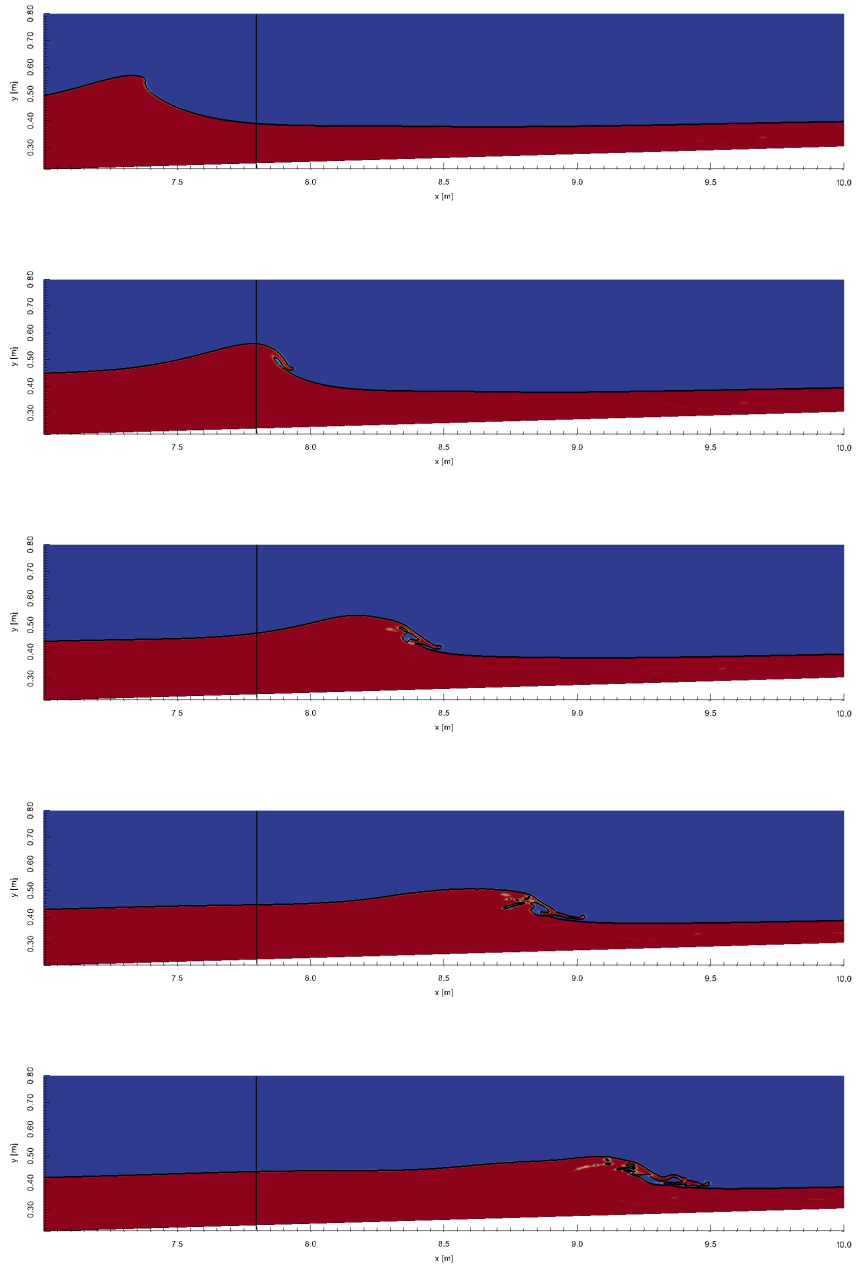

(a)

(b)

(c)

(d)

(e)

Figure 11: Plunging breaker on a 1 : 35 ramp. The contour variable is the volume fraction. The time step between the snapshots is $T/10$. The vertical line shows the position $x_b = 7.79$m of expected breaking, according to the measurements of Ting and Kirby (1994, 1996).

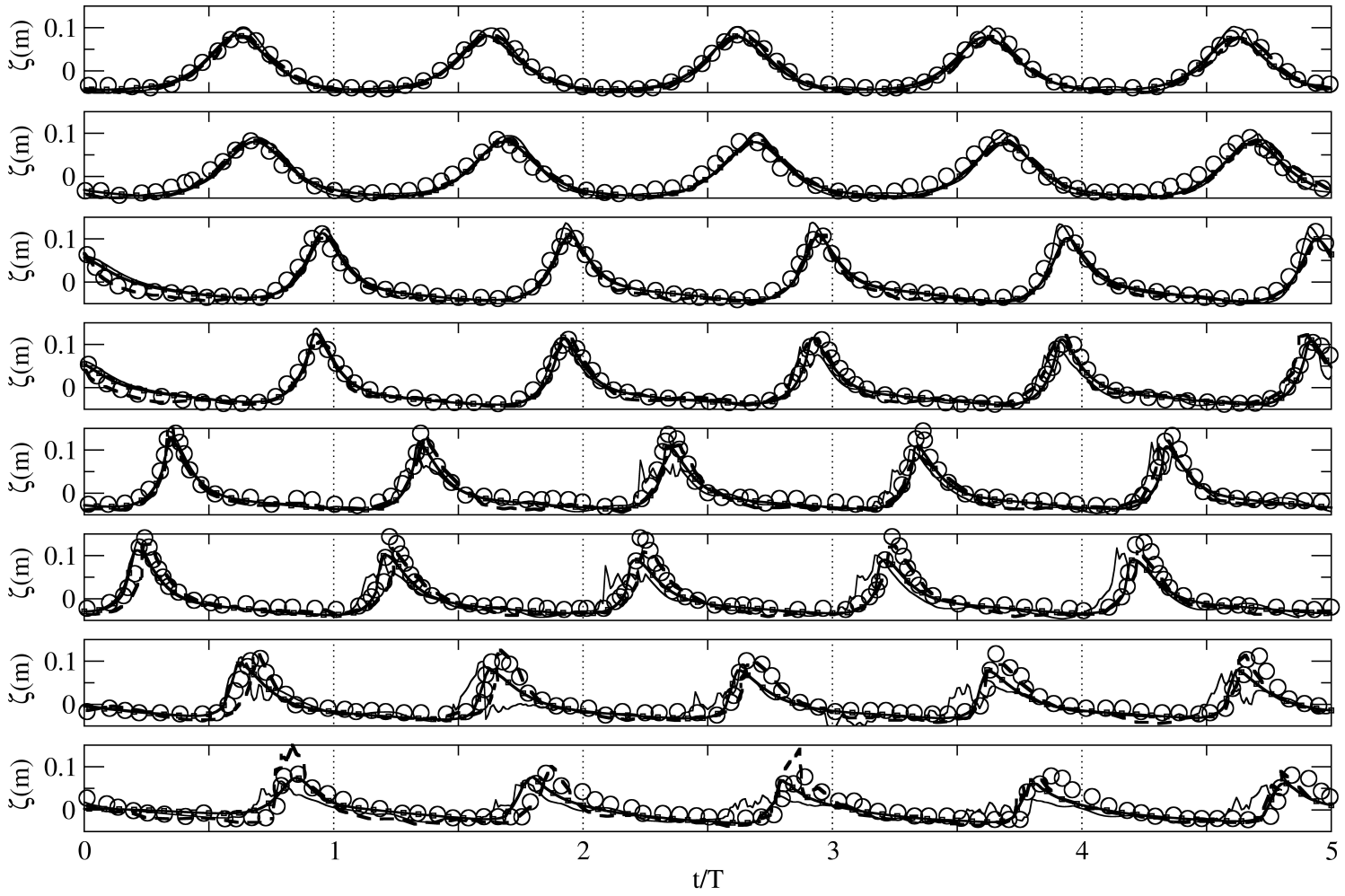

Figure 12: Spilling breaker on a 1 : 35 ramp. Comparison between experimental (Ting and Kirby (1996) as reported in Chella et al. (2015)), numerical results from Chella et al. (2015) and present numerical results. Free surface elevation at 8 gauges along the ramp. $x = -1.5, -0.5, 4.5, 5.5, 6.0, 6.5, 7.0, 8.0$ m (top-down); empty circles = experiments; thick solid line with squares= free surface profile from the present simulation with turbulence model; thin solid line= free surface profile from the present simulation without turbulence model, dashed line = results from Chella et al. (2015).

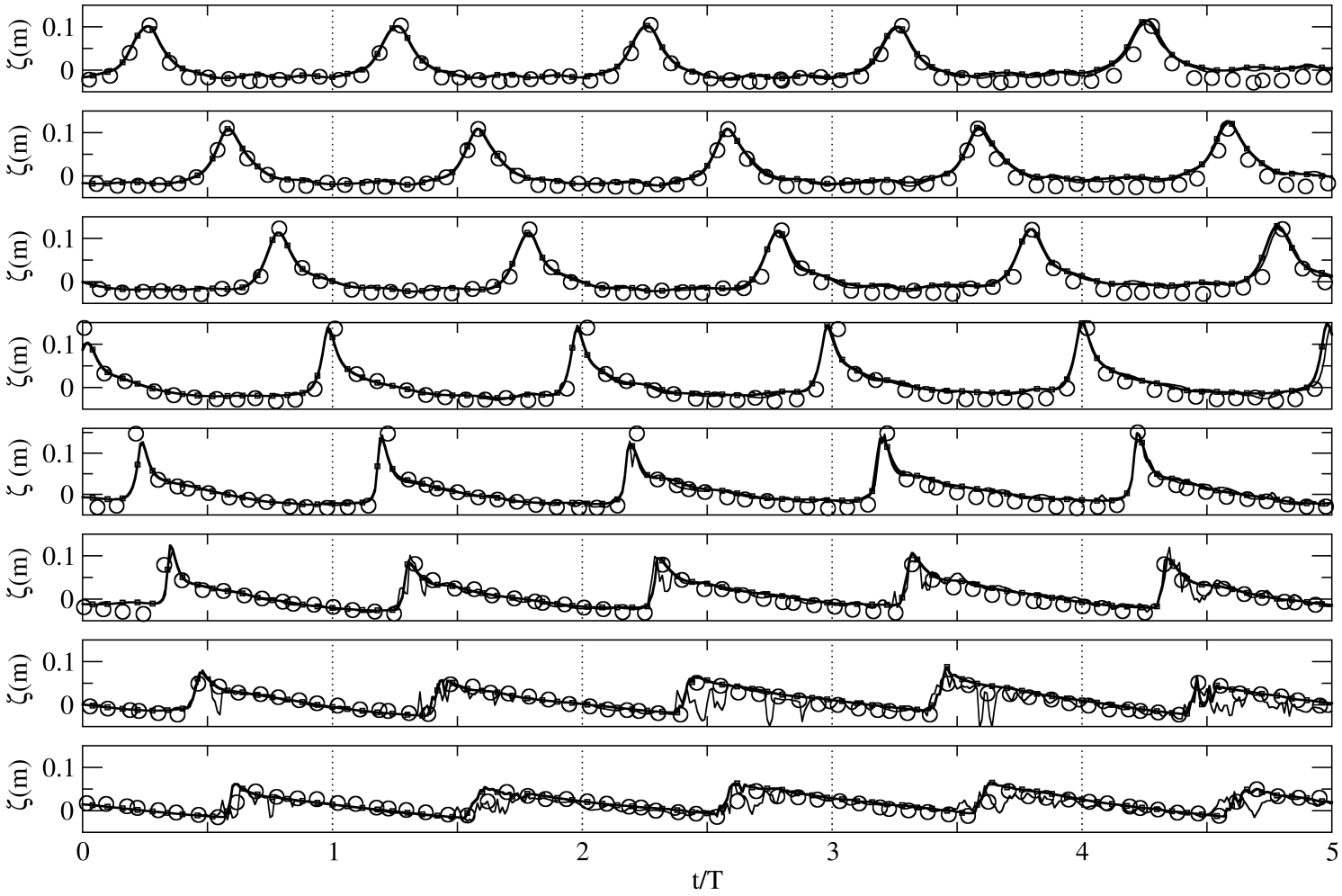

Figure 13: Plunging breaker on a 1 : 35 ramp. Comparison between experimental (Ting and Kirby (1996) as reported in Xie (2013)) and present numerical results. Free surface elevation at 8 gauges along the ramp. x = -1.5, 2, 4, 6, 8, 9, 10, 11 m (top-down); empty circles = experiments; thick solid line with squares= free surface profile from the present simulation with turbulence model; thin solid line= free surface profile from the present simulation without turbulence model.

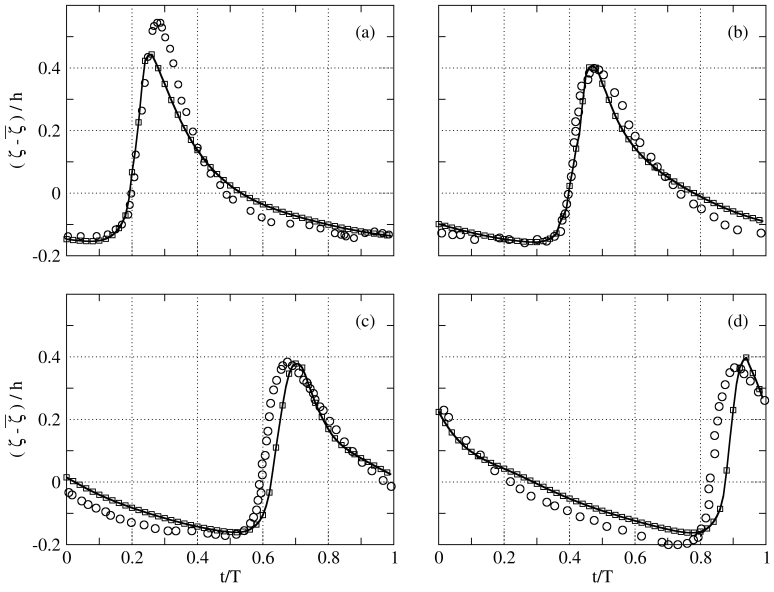

Figure 14: Spilling breaker on a 1 : 35 ramp. Comparison between experimental (Ting and Kirby, 1996) and present numerical results. Phase averaged free surface elevation at 4 gauges along the ramp. (a) x = 7.275m, (b) 7.885m, (c) 8.495m, (d) 9.110m; empty circles = experiments; solid line with squares= free surface profile from the simulation with turbulence model.

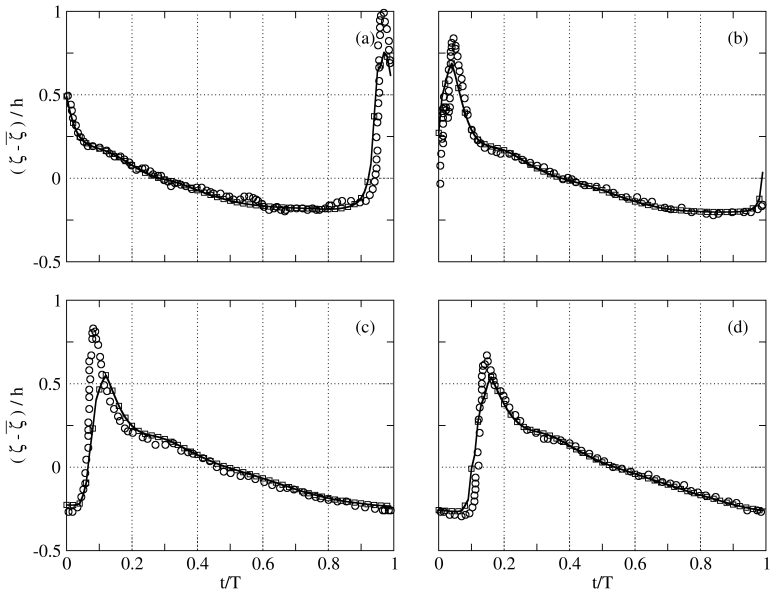

Figure 15: Plunging breaker on a 1 : 35 ramp. Comparison between experimental (Ting and Kirby, 1995) and present numerical results. Phase averaged free surface elevation at 4 gauges along the ramp. (a) $x = 7.795$m, (b) 8.345m, (c) 8.975m, (d) 9.295m; empty circles = experiments; solid line with squares= free surface profile from the simulation with turbulence model.

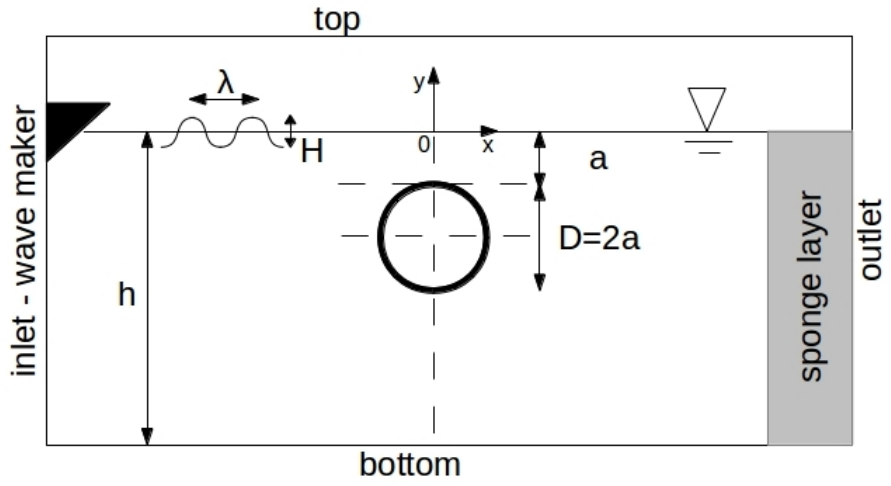

Figure 16: Regular wave breaking over a submerged circular cylinder: schematic representation.

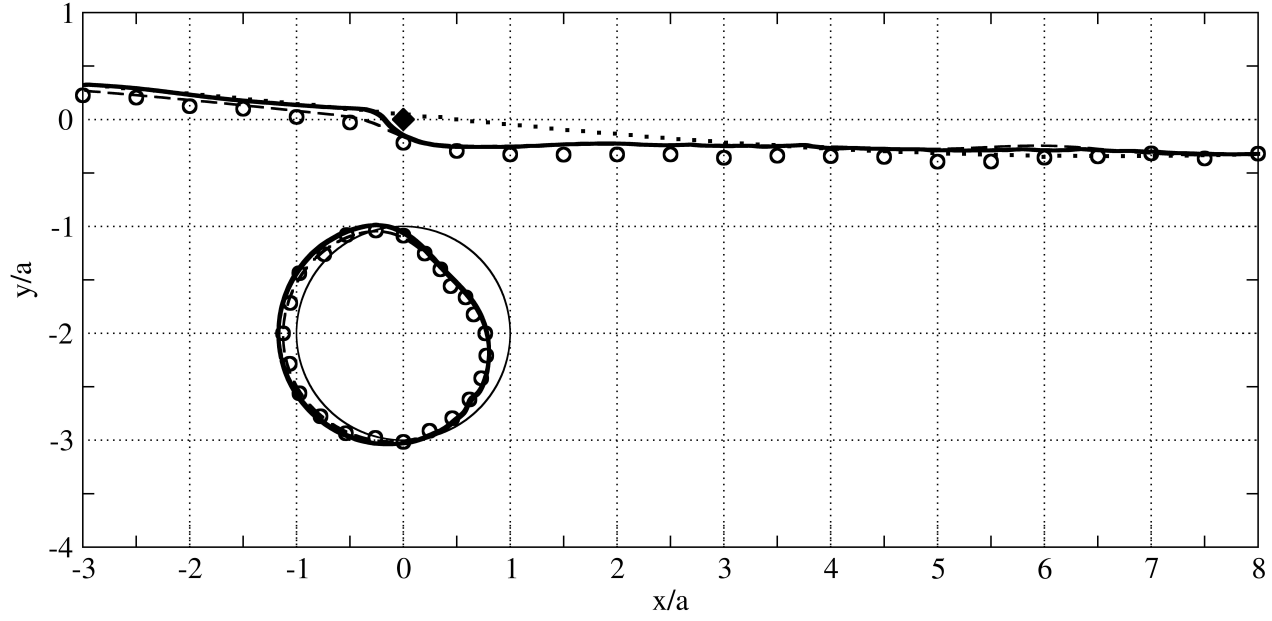

Figure 17: $t/T = 0/8$.

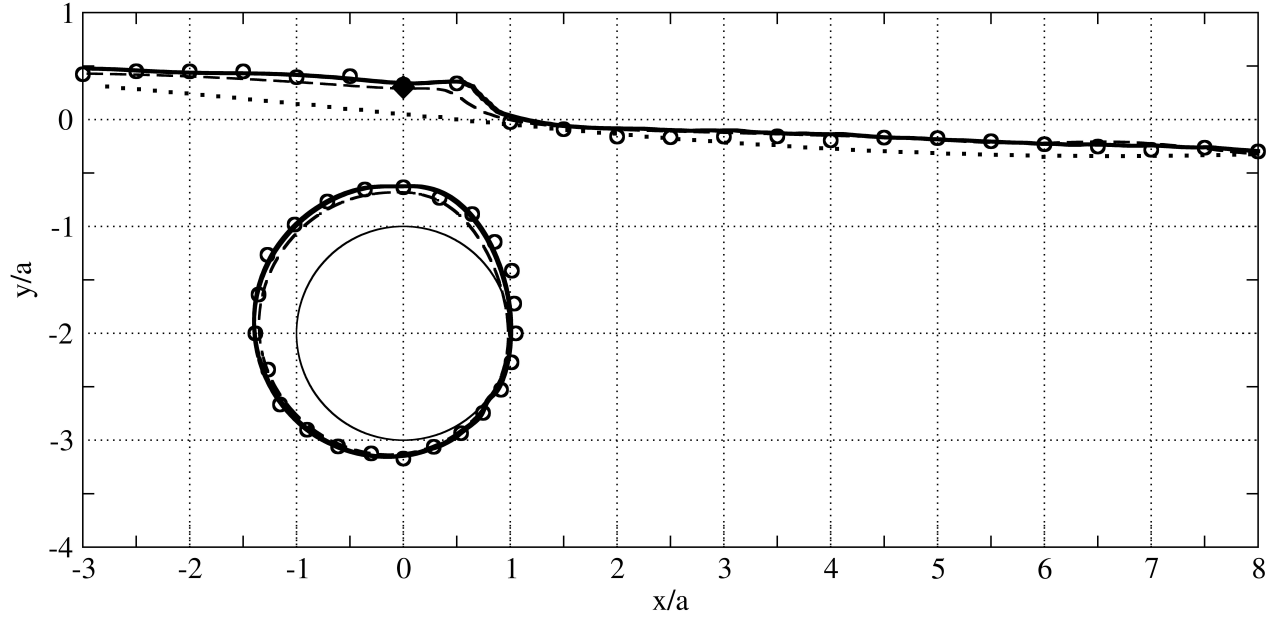

Figure 18: $t/T = 1/8$.

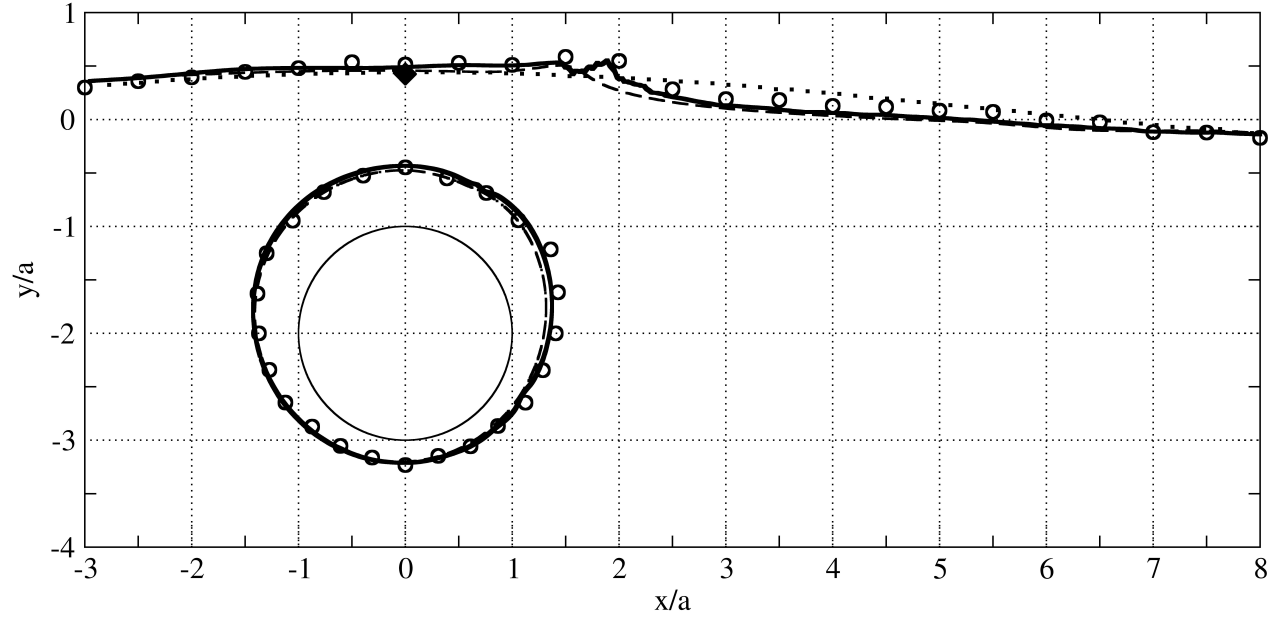

Figure 19: $t/T = 2/8$.

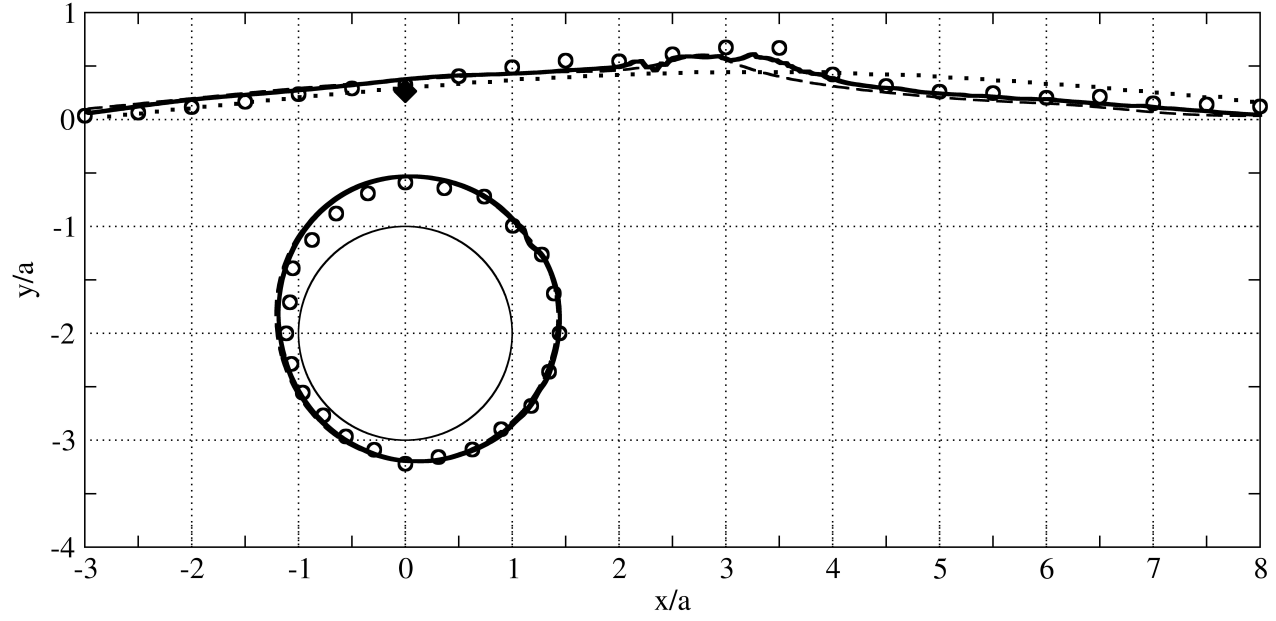

Figure 20: $t/T = 3/8$.

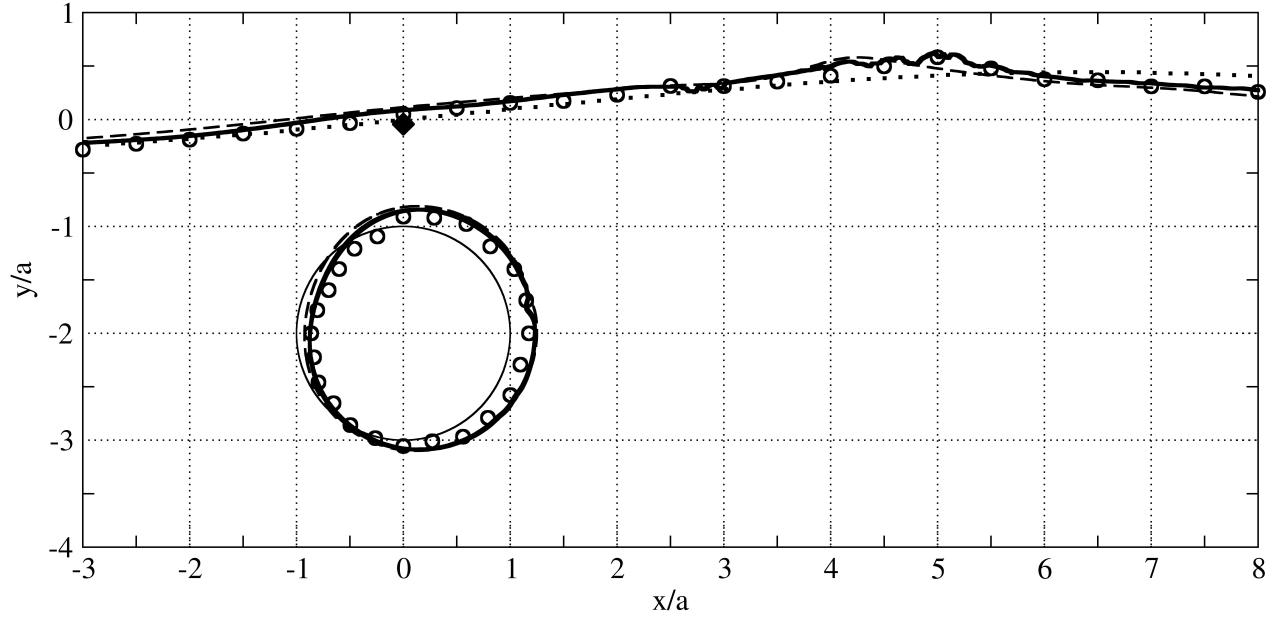

Figure 21: $t/T = 4/8$.

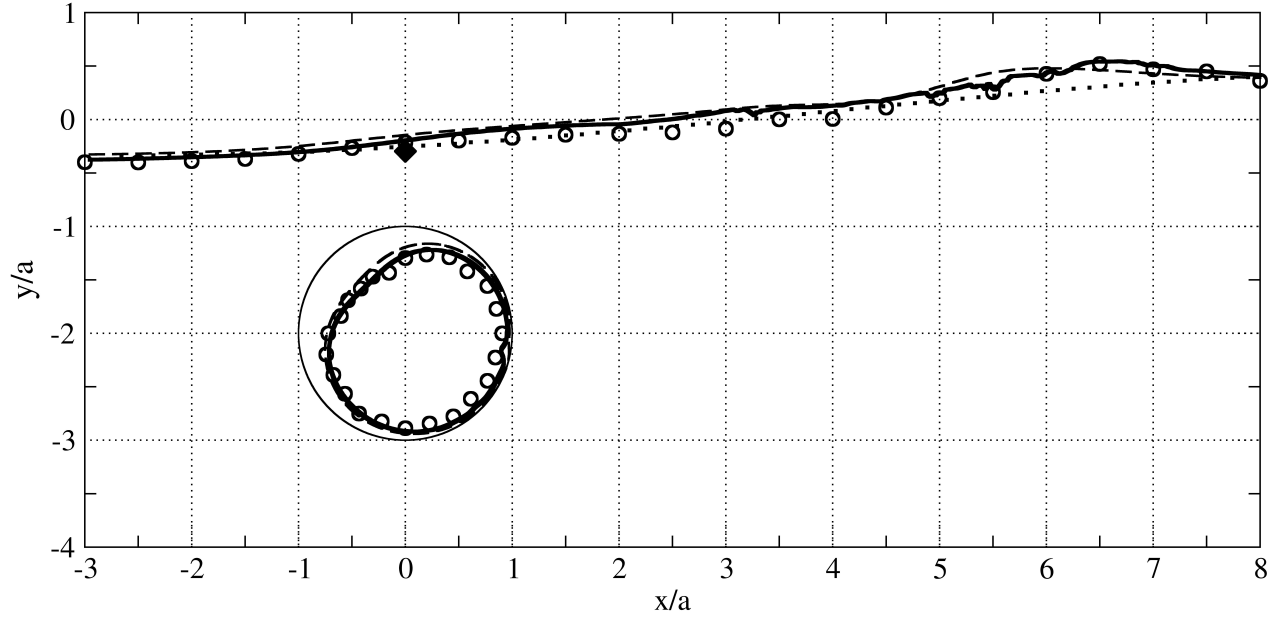

Figure 22: $t/T = 5/8$.

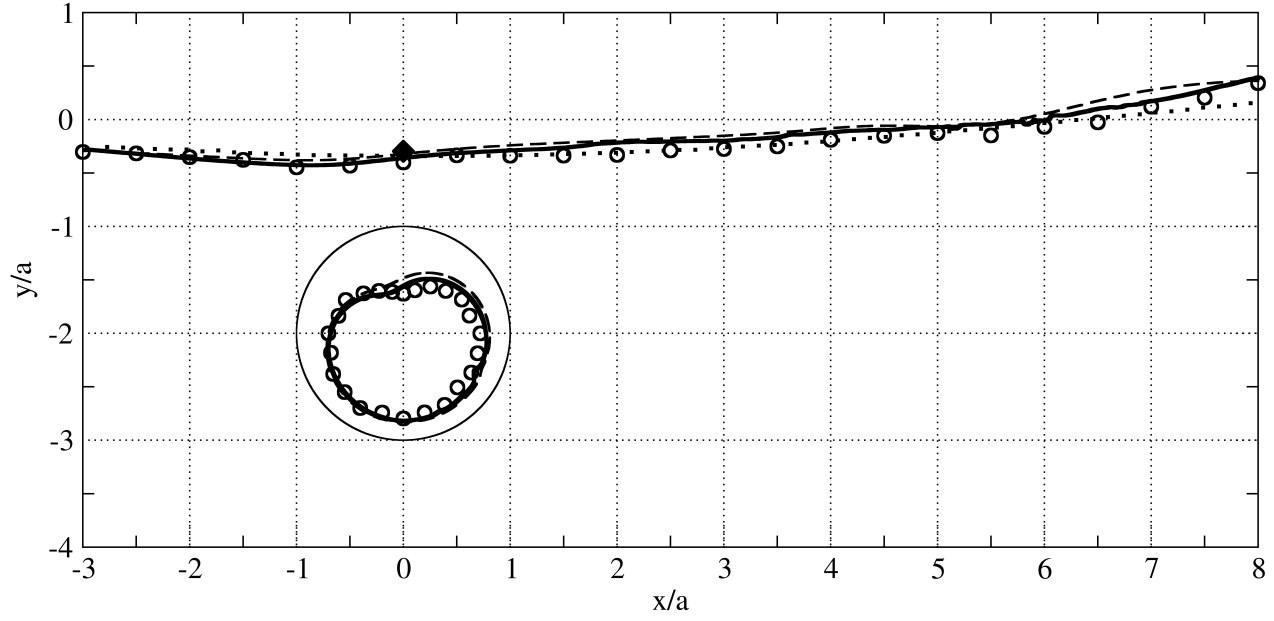

Figure 23: $t/T = 6/8$.

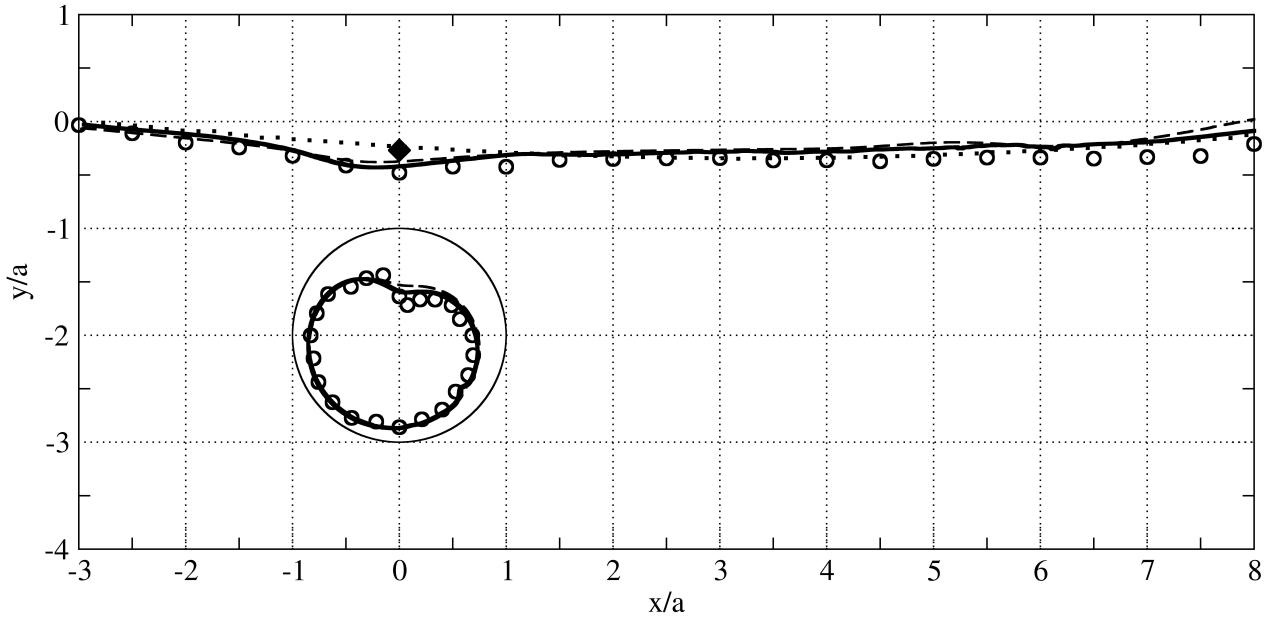

Figure 24: $t/T = 7/8$. Wave elevations at $t/T = j/8$, with $j = 0, 1, 2, \ldots 7$. Dotted line = incident wave profile (simulated separately); thick solid line = free surface elevation and dynamic pressure without turbulence model, dashed line = free surface elevation and dynamic pressure with turbulence model; solid rhombus = experimental (undisturbed) wave elevation at the cylinder axis, empty circles = free surface elevation and dynamic pressure measurements (Contento and Codiglia, 2001).

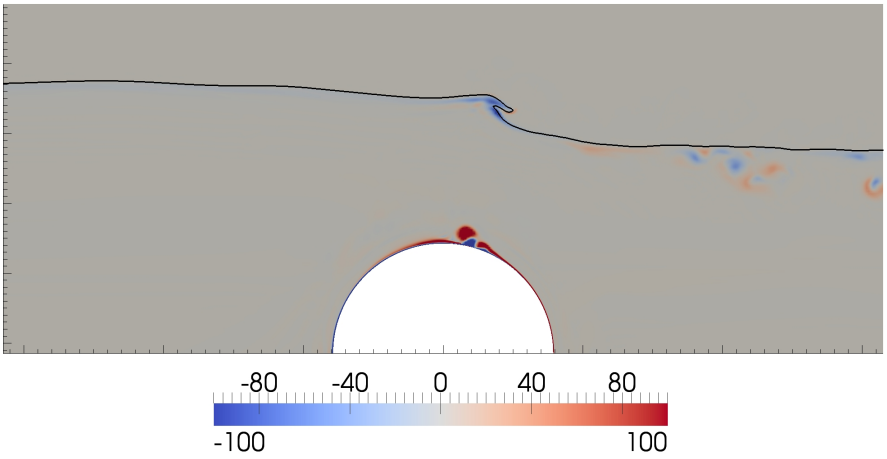

(a)

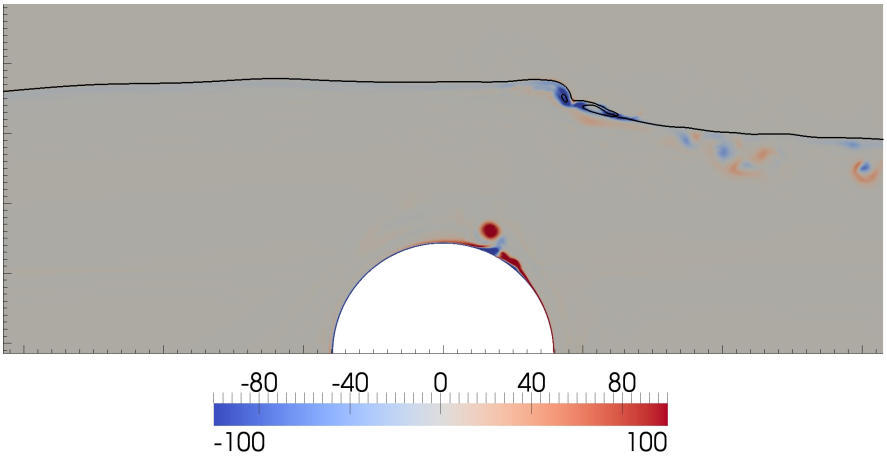

(b)

Figure 25: Contour plot of non-dimensional vorticity at $t/T = 9/80$ (without turbulence model) on (a) and at $t/T = 15/80$ on (b).

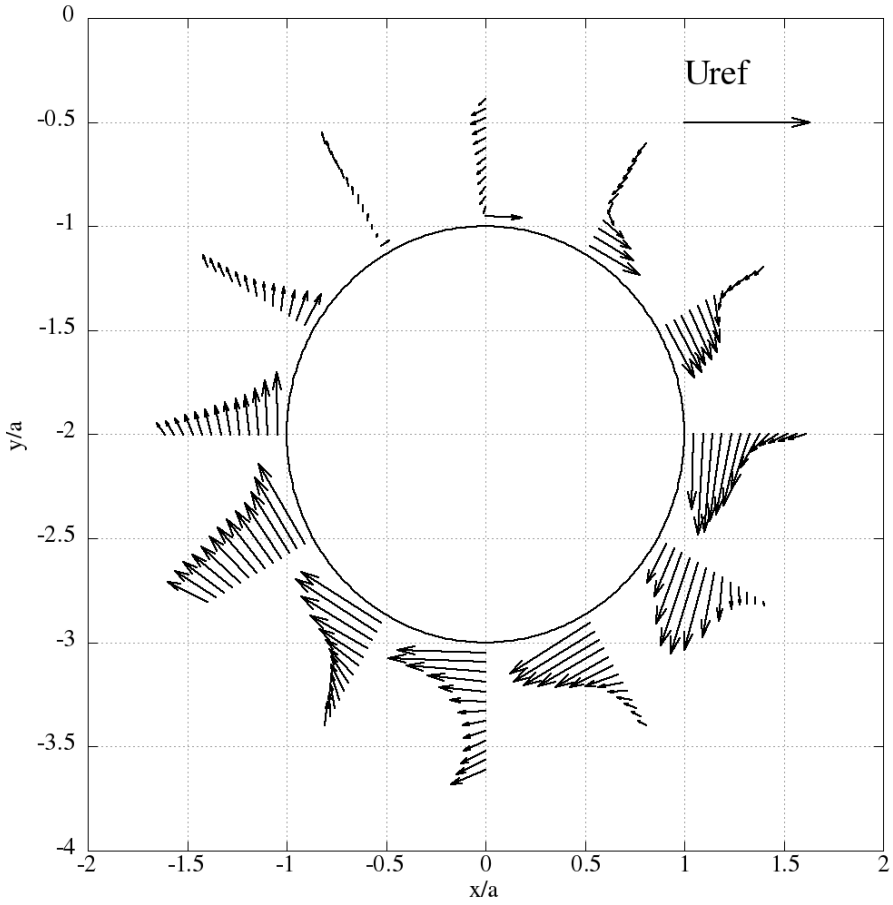

Figure 26: Velocity field close to the cylinder surface, averaged over 4 complete incident wave periods. The reference velocity U_{ref} corresponds to the velocity used to define di KC number.

12. References

Celik, I.,B., Ghia, U., Roache, P.J., Freitas, C.,J., Coleman, H. and Raad, P.,E., 2008. Procedure for Estimation and Reporting of Uncertainty Due to discretization in CFD Applications. Journal of Fluids Engineering, 130, N 7.

Chaplin, J.R., 1984. Mass transport around a horizontal cylinder beneath waves. *Journal of Fluid Mechanics*, 140, 175–187.

Chaplin, J.R., 1984. Forces on a horizontal cylinder below waves. *Journal of Fluid Mechanics*, 147, 449–464.

Chaplin, J.R., 1992. Orbital flow around a circular cylinder. Part 1. Steady streaming in non-uniform conditions. *Journal of Fluid Mechanics*, 237, 395–411.

Chaplin, J.R., 1993. Orbital flow around a circular cylinder. Part 2. Attached flow at larger amplitudes. *Journal of Fluid Mechanics*, 246, 397–418.

Chaplin, J.R., Ikeda, Y., 1999. Viscous Forces on Offshore Structures and Their Effects on the Motion of Floating Bodies, Proc. 9^{th} Int. Offshore and Polar Engineering Conference, Brest, France, May 30 June 4, Vol. III, pp. 1-11.

Chella, M.,A., Bihs, H., Myrhaug, D. and Muskulus, M., 2015. Breaking characteristics and geometric properties of spilling breakers over slopes. *Coastal Engineering*, 95, 4-19.

Chen Y.G., Price W.G. and Temarel P., 2011. An anti-diffusive VOF method for simulation of free surface wave over a bump *IWWWFB*, Proceedings.

Chen, L.,F., Zang, J., Hillis, A.,J., Morgan, G.,C.,J. and Plummer, A.,R., 2014 Numerical investigation of wave structure interaction using OpenFOAM. *Ocean Engineering*, 88, 91-109.

Christensen, E.D., 2006. Large Eddy Simulation of Spilling and Plunging Breakers. Int. Journal for Coastal, Harbor and Offshore Engineers, 53, 463-485.

Clement, A., 1996. Coupling of two absorbing boundary conditions for 2d time-domain simulations of free surface gravity waves. Journal of Computational Physics, 126:139-151.

Contento G. and Codiglia R., 2001, Non lineaar free surface induced pressure on a submerged horizontal circular cylinder at low Keulegan-Carpenters numbers. Applied Ocean Research, 23, 175-185.

Contento, G., D'Este, F., Codiglia, R., 2003. Numerical Study on the Non-linear Behaviour of Steep Isolated Unidirectional Waves, 13^{rd} International Conference on Offshore and Polar Engineering – ISOPE'2003, May 2003, Honolulu – Hawaii, USA, Vol. 3, pp. 100-105.

Contento G., Lupieri G, Jasak H. and Vukčević V., 2015. Numerical Study of Unsteady Breaking Waves Induced by a Submerged Hydrofoil at Steady Forward Speed. Proceedings NAV 2015, 17^{th} International Conference on Ships and Shipping Research, accepted for presentation.

De Blasi, P., Romano, G.P., Di Felice, F., Lalli, F., 2000. Experimental Study of Breaking Wave Flow Field Past a Submerged Hydrofoil by LDV. Int. J. of Offshore and Polar Engineering, 10, 263-268.

Duncan, J.H., 1981. An experimental investigation of breaking waves produced by a towed hydrofoil. Proc. R. Soc. Lond. A 377, 331-348.

Duncan, J.H., 1983. The breaking and non-breaking wave resistance of a two-dimensional hydrofoil. J. Fluid Mech. 126, 507-520.

Duncan, J.H., 2001. Spilling breakers. Annual Rev. Fluid Mech., 33, 519-547.

Fenton, J.D., 1998. The cnoidal theory of water waves. In Developments in Offshore Engineering. Ed. J.B. Herbich, Gulf: Huston, (Chapter 2, pp. 1-34).

Hedges, T.S., 1995. Regions of validity of analytical wave theories. Proc. Inst. Civ. Engnrs, Water, Maritime and Energy, 112, 111-114.

Higuera P., Lara L.J., and Losada I.J., 2013. Realistic wave generation and active wave absorption for Navier-Stokes models application to OpenFOAM. Coastal Engineering, 71:102-118.

Higuera P., Lara L.J., and Losada I.J., 2013. Simulating coastal engineering processes with OpenFOAM. Coastal Engineering, 71:119-134.

Hirt, C.W., Nichols, B.D., 1981. Volume of Fluid (VOF) Method for the Dynamics of Free Boundaries. J. Comput. Physics, 39, 201-225.

Iaccarino, G., Ooi, A., Durbin, P.A., Behnia, M., 2003. Reynolds Averaged Simulation of Unsteady Separated Flow. Int. Journal of Heat and Fluid Flow, 24, 147-156.

IITC - Specialist Committee on CFD in Marine Hydrodynamics, 2014. Proceedings - Volume II. 27th International Towing Tank Conference (ITTC), Copenhagen.

Jacobsen N.G., Fuhrman D.R., and Fredsøe J., 2012. A wave generation toolbox for the open-source CFD library: OpenFOAM. International Journal for Numerical Methods in Fluids, 70(9):1073-1088.

Kimmoun O. and Branger H., 2007. A particle image velocimetry investigation on laboratory surf-zone breaking waves over a sloping beach. J. Fluid Mech., 588, 353-397.

Lilly D.K., 1969. Numerical simulation of two-dimensional turbulence. The Physics of Fluids Supplement II, 240-249.

Lubin, P., Vincent, S., Abadie, S., Caltagirone, J., 2006. Three-dimensional Large Eddy Simulation of air entrainment under plunging breaking waves. Coastal Engineering, 53, 631-655.

Lubin, P., Glockner S., Kimmoun O., Branger H., 2011. Numerical study of the hydrodynamics of regular waves breaking on a sloping beach. Eur. J. Mech. B/Fluids, 30, 552-564.

Lupieri, G., Del Puppo, N., Morgut, M., Contento, G., Nobile, E., Genuzio, H., Lavini, G., 2012. OpenSHIP Project - Numerical Predictions of Ship and Propeller Hydrodynamics by OpenSource CFD: Results from Preliminary Benchmark Tests. Proceedings NAV 2012, 17^{th} International Conference on Ships and Shipping Research and Advancing with Composite 2012 Symposium, (on CD).

Lupieri, G., Puzzer, T., Contento, G., 2014. Numerical study of the wave-wave interaction by viscous flow simulations with OpenFOAM. Proceedings, 21^{th} Symposium Theory and Practice of Shipbuilding SORTA Oct. 2-4, 2014, Baška, Island of Krk, Croatia.

Lupieri, G., Contento, G., 2015. Free surface - vortex interaction in the wavy flow past a submerged horizontal circular cylinder at low Keulegan-Carpenter numbers. Under review.

Maki, K., 2011. Ship Resistance Simulations with OpenFOAM. 6^{th} OpenFOAM Workshop, The Pennsylvania State University State College, PA, USA, $13-16$ June.

Menter, F.R., 1994. Two-Equation Eddy-Viscosity Turbulence Models for Engineering Applications. AIAA Journal, 8, 1598-1605.

Muscari R., Di Mascio, A., 2004. Numerical Modeling of Breaking Waves Generated by a Ship's Hull. Journal of Marine Science and Technology. 9, 158-179.

OpenFOAM, OpenFOAM User Guide. OpenCFD Ltd, 2012.

Rhee, S.H., Stern, F., 2002. RANS Model for Spilling Breaking Waves. ASME, 124, 424-432.

Roache, P.J. 1997. Quantification of uncertainty in computational fluid dynamics. Annual Rev. Fluid Mech., 29, 123-160.

Rusche, H., 2002. Computational Fluid Dynamics of Dispersed Two - Phase Flows at High Phase Fractions. Imperial College of Science, Technology & Medicine, London.

Smith, K., R., 2009 Computation of viscous multiphase hydrodynamics and ship motions during wave slap events and wave excited roll.
Aster of Science Thesis in Mechanical Engineering at Pennsylvania State University.

Swan, C., 2014. Group discussion on wave quality in wave basins and accurate models for the design wave kinematics. 27^{th} International Towing Tank Conference (ITTC), Copenhagen.

Tian, Z., Perlin, M., Choi, W., 2012. An eddy viscosity model for two-dimensional breaking waves and its validation with laboratory experiments. Physics of Fluids, 24, 036601.

Ting, F.C.K., Kirby, J.T., 1994. Observation undertow and turbulence a of in laboratory surf zone. Coastal Engineering, 24, 51-81.

Ting, F.C.K., Kirby, J.T., 1995. Dynamics of surf-zone turbulence in a strong plunging breaker. Coastal Engineering, 24, 177-204.

Ting, F.C.K., Kirby, J.T., 1996. Dynamics of surf-zone turbulence in a spilling breaker. Coastal Engineering, 27, 131-160.

Xie, Z., 2013. Two phase flow modelling of spilling and plunging breaking waves. Applied Mathematical Modelling, 37, 3698-3713.

Wang, H., Huang, C., Wu, J., 2007. Simulation of a 3D Numerical Viscous Wave Tank. Journal of Engineering Mechanics, 133, 761-772.

Zhao, Q., Armfield, S., Tanimoto, K. Numerical simulation of breaking waves by a multiscale turbulent model. Coastal Engineering, 51, 53-80, 2004.

Zhao, Q., Armfield, S. Recent Advances in Turbulence Modeling for Unsteady Breaking Waves. Advances in Numerical Simulation of Nonlinear Water Waves, in Advances in Coastal and Ocean Engineering, 11, 605-640, Ed. World Scientific., 2010.